

1 **Intensive photochemical oxidation in the marine atmosphere:**
2 **Evidence from direct radical measurements**

3 Guoxian Zhang^{1,2}, Renzhi Hu^{1, *}, Pinhua Xie^{1,2,3, **}, Changjin Hu¹, Xiaoyan Liu⁴,
4 Liujun Zhong¹, Haotian Cai¹, Bo Zhu⁵, Shiyong Xia⁵, Xiaofeng Huang⁵, Xin Li⁶,
5 Wenqing Liu¹

6 ¹ Key Laboratory of Environment Optics and Technology, Anhui Institute of Optics and Fine
7 Mechanics, HFIPS, Chinese Academy of Sciences, Hefei, China

8 ² University of Science and Technology of China, Hefei, China

9 ³ College of Resources and Environment, University of Chinese Academy of Science, Beijing,
10 China

11 ⁴ School of Pharmacy, Anhui Medical University, Hefei, China

12 ⁵ Key Laboratory for Urban Habitat Environmental Science and Technology, School of
13 Environment and Energy, Peking University Shenzhen Graduate School, Shenzhen, China

14 ⁶ State Key Joint Laboratory of Environmental Simulation and Pollution Control, College of
15 Environmental Sciences and Engineering, Peking University, Beijing, China

16

17 ***Correspondence to:** Renzhi Hu, Key Laboratory of Environment Optics and
18 Technology, Anhui Institute of Optics and Fine Mechanics, HFIPS, Chinese Academy
19 of Sciences, Hefei, China

20 ****Correspondence to:** Pinhua Xie, University of Science and Technology of China,
21 Hefei, China

22 **Email addresses:** rzhu@aiofm.ac.cn (Renzhi Hu); phxie@aiofm.ac.cn (Pinhua Xie)

23

24 **Abstract:** Comprehensive observations of hydroxyl (OH) and hydroperoxy (HO₂)
25 radicals were conducted in October 2019 at a coastal continental site in the Pearl
26 River Delta (YMK site, 22.55°N, 114.60°E). The ~~average~~ daily maximum OH and
27 HO₂ concentrations were $(4.7\text{--}9.5) \times 10^6 \text{ cm}^{-3}$ and $(4.2\text{--}8.1) \times 10^8 \text{ cm}^{-3}$, respectively.
28 The synchronized air mass transport from the northern cities and the South China Sea
29 exerted a time-varying influence on atmospheric oxidation. Under a typical ocean-
30 atmosphere (OCM), reasonable measurement model agreement was achieved for both
31 OH and HO₂ using a 0-D chemical box model incorporating the regional atmospheric
32 chemistry mechanism version 2-Leuven isoprene mechanism (RACM2-LIM1)-, with
33 daily averages of $4.5 \times 10^6 \text{ cm}^{-3}$ and $4.9 \times 10^8 \text{ cm}^{-3}$, respectively. Land mass (LAM)
34 influence promoted more active photochemical processes, with daily averages of 7.1
35 $\times 10^6 \text{ cm}^{-3}$ and $5.2 \times 10^8 \text{ cm}^{-3}$ for OH and HO₂, respectively. Heterogeneous uptake
36 had certain effects on HOx chemistry, but the influence of the halogen mechanism
37 was limited by NOx level. –Intensive photochemistry occurred after precursor
38 accumulation, allowing local net ozone production comparable with surrounding
39 suburban environments (5.52 ppb/h during the LAM period). ~~The~~ Rapid oxidation
40 process was accompanied by a higher diurnal nitrous acid (HONO) concentration (>
41 400 ppt). After a sensitivity test, HONO-related chemistry elevated the ozone
42 production rate by 33% and 39% during the LAM and OCM periods, respectively.
43 The nitric acid (P(HNO₃)) and sulfuric acid (P(H₂SO₄)) formation rates also increased
44 simultaneously (~43% and ~48% for LAM and OCM sectors, respectively). Without
45 the HONO constraint, After a sensitivity test, HONO-related chemistry elevated the
46 ozone production rate by 33% and 39% during the LAM and OCM periods,
47 respectively, while the nitric acid and sulfuric acid formation rates were 52% and 35%
48 higher, respectively. The simulated O₃ decreased from ~75 ppb to a global
49 background (~35 ppb), and daytime daytime-HONO and ozone concentrationss
50 reduced to a low level a low level (~70 ppt and ~35 ppb). –without the HONO
51 constraint. This work challenges the conventional recognition of the MBL in a
52 complex atmosphere. For coastal cities, the particularity of the HONO chemistry in

53 ~~the MBL~~ tends to influence the ozone-sensitive system and eventually magnifies the
54 background ozone. Therefore, the promotion of oxidation by elevated precursor
55 ~~concentrations~~ deserves a lot of attention ~~is worth considering~~ when aiding pollution
56 mitigation policies. ~~formulating emission reduction policies~~.

57 **Keywords:** FAGE-LIF; OH and HO₂ radicals; Atmospheric oxidation; Marine
58 boundary layer; Precursors;

59

1 Introduction

The marine boundary layer (MBL) occupies 71% of the planetary boundary layer, is a massive active carbon sink on Earth, and plays an irreplaceable role in coping with global climate change (Stone et al., 2012; Woodward-Massey et al., 2022b; Liu et al., 2022a). As a typical background atmosphere on the Earth, the MBL is equivalent to a natural smog chamber with limited anthropogenic emissions and is characterized by low NO_x (the sum of nitric oxide (NO) and nitrogen dioxide (NO₂)) and non-methane hydrocarbons (NMHCs) under a layer of clean air (Woodward-Massey et al., 2022b). The lifetime of OH radical, a key oxidant, is on the order of a few hundred milliseconds (Fuchs et al., 2012). Due to the scarcity of oxidation precursors, including nitrous acid (HONO), formaldehyde (HCHO), and NMHCs, the reaction between O¹D and water vapor generally dominates the radical initiation pathway in the marine environment. For example, in a tropical boundary layer observation experiment (reactive halogens in the marine boundary layer, RHaMBLe), ozone photolysis was found to account for 70% of the OH radical source based on the master chemical mechanism (MCM) (Whalley et al., 2010). The vital role of ozone photolysis is contrasting with typical polluted and semi-polluted areas investigated in a series of field campaigns, in which the propagation routes were found to dominate the radical source (Yang et al., 2021a; Tan et al., 2019a). Therefore, studying the radical chemistry in the MBL provides a valuable opportunity to test the current understanding of atmospheric oxidation mechanisms in a natural setting.

Since the earliest observations off the coast of northern Norfolk in the Weybourne Atmospheric Observatory Summer Experiment in June 1995 (WAOSE95), more observations and simulations of radical chemistry in the MBL environment have been conducted using ground-based, airborne, and shipborne instruments (Qi et al., 2007; Kanaya et al., 2002; Kanaya et al., 2001; Mallik et al., 2018; Woodward-Massey et al., 2022a; Carpenter et al., 2011; Grenfell et al., 1999; Brauers et al., 2001; Whalley et al., 2010). Most field measurements have yielded well-reproduced OH and HO₂ concentration profiles via chemical mechanisms, with differences of within ~20%.

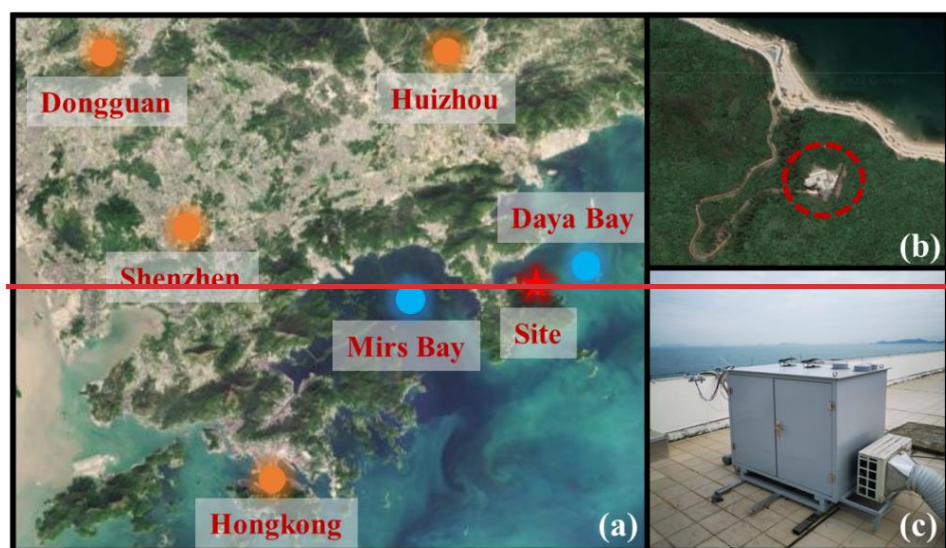
89 However, the base model is not sufficient to describe the radical chemistry in some
90 exceptional cases, especially in regard to the HO₂ radical. Considering the practical
91 association between halogen (Cl, Br, and I) chemistry and heterogeneous chemistry in
92 marine new particle formation, particularly the involvement of heterogeneous iodine-
93 organic chemistry, exploring the synchronous influence of these mechanisms on HO_x
94 (OH and HO₂) radical chemistry in the MBL region is a worthy endeavor (Xu et al.,
95 2022; Huang et al., 2022). The mixing of air masses of continental and marine origins
96 can lead to more variability in radical concentrations. During seasonal measurements
97 of both OH and HO₂ in the Atlantic Ocean, variance analysis indicated that around 70%
98 of the variance of OH and HO₂ was due to diurnal behavior (in the form of photolysis
99 frequency), while the remaining variance was attributed to long-term seasonal cycles
100 (in the form of the changes in O₃, CO and air mass contribution) (Vaughan et al.,
101 2012).

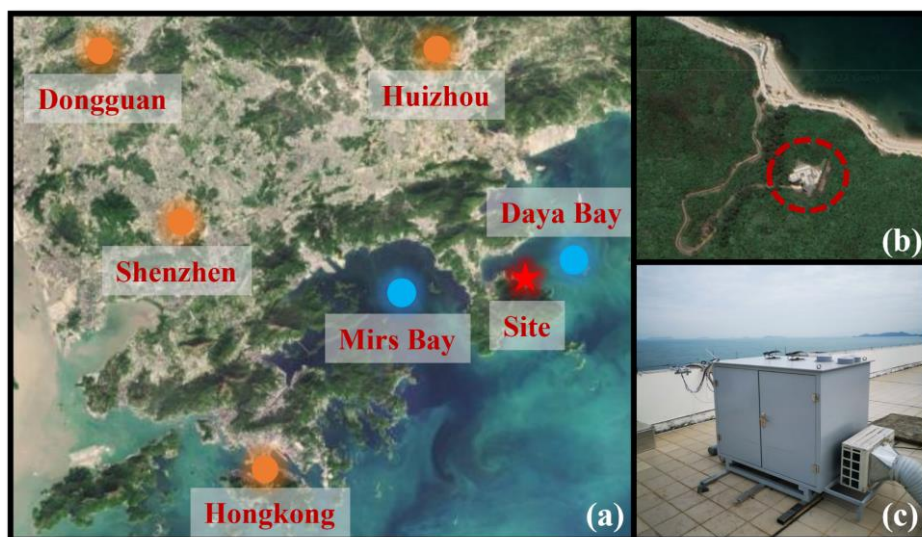
102 The Chinese economy has undergone rapid development in recent years, and the
103 co-occurrence of primary and secondary regional pollution has become a severe
104 problem (Lu et al., 2019; Liu et al., 2022c). The interactions between air pollutants
105 from upwind cities, shipping vessels, and other anthropogenic emissions lead to
106 precursor accumulation (Sun et al., 2020; Zeren et al., 2022). The background ozone
107 concentration in key regions of China has increased year by year, highlighting the
108 significant influence of anthropogenic activities on the atmospheric oxidation in
109 background regions in China (Wang et al., 2009; Chen et al., 2022). However, little
110 research has been dedicated to the radical chemistry and oxidation mechanism in
111 regions with both coastal and continental features. To fill this research gap, in this
112 study, a field campaign was conducted on photochemistry in the MBL at a coastal site
113 in the Pearl River Delta. The OH and HO₂ radicals associated with other related
114 species were measured in October 2019, and the radical-related oxidation process was
115 identified to determine the photochemical efficiency in the marine atmosphere.

116 **2 Materials and methods**

117 2.1 Site description

118 As shown in Fig. 1(a), this observation campaign lasted for 11 days from
119 October 18 to October 28, 2019, in Yangmeikeng (YMK, 22.55°N, 114.60°E), a
120 coastal site in Shenzhen, Pearl River Delta. As the core city of the Greater Bay Area,
121 Shenzhen is bordered by Dongguan to the north, Huizhou to the east, and Hong Kong
122 to the south. The YMK site is on the Dapeng Peninsula, to the southeast of Shenzhen,
123 between Mirs Bay and Daya Bay. As it is adjacent to the port of Hong Kong,
124 precursors from ship emissions may influence the atmospheric chemistry. The site is a
125 part of Shenzhen Ecological Monitoring Center station, approximately 35 m above
126 sea level, and the sea is approximately 150 m to the east. No apparent local emissions
127 exist, and the surrounding forest is lush (Fig. 1(b)). Previous literatures reported the
128 monoterpene concentration in the YMK site, with a daily mean of 0.187 ppb (Zhu et
129 al., 2021). Abundant biogenic emissions will likely influence the local chemistry. In
130 addition to anthropogenic and vegetation emissions, the site is also affected by the
131 synchronization of plumes from northern cities and the South China Sea (Niu et al.,
132 2022; Xia et al., 2021). Due to its significant time-varying pollution characteristics,
133 this area is an ideal site for studying the effects of plume transport on atmospheric
134 oxidation.





136
137 **Fig. 1.** Details of the observation site.(a) The location of the measurement site and surrounding cities. The satellite
138 map data is extracted from Google Earth.(b) Th close shot of the measurement site location.(c) The actual image
139 for the LIF-Box.

140 Using the hybrid single-particle Lagrangian integrated trajectory (HYSPLIT)
141 model, the 24-h backward trajectories on special days were obtained. In Fig. S1, the
142 red, blue, and green trajectories represent the results at altitudes of 100, 500, and 1000
143 m above ground level, respectively. Two typical transportation pathways dominated
144 the air parcels. One originated from the northern megacities in the Pearl River Delta
145 (defined as the land mass, LAM), especially on October 18, 19, and 27. In contrast, a
146 clean air mass from the east or northeast was mainly transported to the observation
147 site from the ocean (defined as the ocean mass, OCM), with representative episodes
148 on October 22, 25, and 26.

150 2.2 Instrumentation

151 2.2.1 HOx radical measurements

152 The OH and HO₂ radicals were measured via laser-induced fluorescence (LIF).
153 The OH radical can be directly measured by exciting the fluorescence using a 308-nm
154 laser. HO₂ is converted into the OH radical via chemical transformation and then
155 detected in the form of OH radical. The self-developed instrument, the Anhui Institute
156 of Optics Fine Mechanics-LIF (AIOFM-LIF), was used to conduct the measurements
157 (Zhang et al., 2022a; Wang et al., 2021; Wang et al., 2019). This system has been used
158 in key regions of China, including the Yangtze River Delta, Pearl River Delta, and

159 Chengdu-Chongqing region, and achieved good performance in a comparison
160 experiment with a LIF system jointly developed by Forschungszentrum Jülich and
161 Peking University (PKU-LIF) (Zhang et al., 2022b).

162 The system and detection interference process have been described in detail in
163 previous studies (Zhang et al., 2022a). Briefly, the system consists of a laser output
164 module, a radical detection module, and a control and data acquisition module. These
165 modules are integrated into a sampling box with constant temperature and humidity
166 control (Fig. 1(c)). The laser output module is a union of an Nd:yttrium-aluminum-
167 garnet (YAG) solid-state laser, a 532-nm laser output, and a tunable dye laser. The
168 radical detection module utilized a single pass laser configuration, and the laser beam
169 was amplified to a diameter of 8 mm. ~~In the radical detection module, the~~ OH and
170 HO₂ fluorescence cells are combined in parallel and share a common axial optical
171 path. The 308-nm laser is introduced into the HO₂ cell first and then into the OH cell
172 via an 8-m fiber. To maintain the detection efficiency, the power in the OH
173 fluorescence cell should be at least 15 mW. In the detection process, a set of lenses
174 was deployed and positioned in front of the microchannel plate detector (MCP) to
175 boost the fluorescence collection capacity. Each MCP detector contains a timing
176 control instrument to optimize the signal-to-noise ratio (SNR) of the fluorescence
177 detection. Efficient ambient air sampling was achieved using an aluminum nozzle (0.4
178 mm orifice), and the pressure in the chamber was maintained at 400 Pa via a vortex
179 vacuum pump (XDS35i, Edwards) to ~~avoid~~reduce fluorescence quenching.

180 A wavelength modulation for the background measurement that periodically
181 switches from an on-resonant state to a non-resonant state has been widely used to
182 obtain spectral zero. Due to the synchronous reaction at 308nm, wavelength
183 modulation is not applicable to ozone photolysis interference. Through laboratory
184 experiments, at 20 mW laser energy, every 1% water vapor concentration and 50 ppb
185 ozone concentration can generate a $2.5 \times 10^5 \text{ cm}^{-3}$ OH concentration. The results in
186 this paper have subtracted the ozone photolysis interference (Fig. S2). In terms of
187 system design, the AIOFM-LIF system incorporates a short-length inlet design to

188 minimize interferences from ozonolysis and other unknown factors (the distance from
189 radical sampling to fluorescence excitation is ~150 mm). The ozone photolysis
190 interference was subtracted according to laboratory experiments. An OH
191 measurement comparison with an interference-free instrument, PKU-LIF, was
192 conducted in a real atmosphere in a previous study (Zhang et al., 2022b). The
193 ozonolysis interference on the measurement consistency of both systems was
194 excluded under high-VOCs condition. Overall, the key parameters related to
195 ozonolysis reactions (O₃, alkenes, isoprene and NO_x) in YMK was similar to that
196 during the intercomparison experiment, implies that the chemical conditions do not
197 favor the generation of potential interference to OH measurement (Table S1). The
198 ozonolysis interference on the measurement consistency of both systems was
199 excluded under high NO_x and high NMHC conditions, confirming the general
200 applicability under complex atmospheric pollution. For HO₂ measurement, the NO
201 gas was mixed with 2% in N₂ to achieve HO₂-to-OH conversion. NO was passed
202 through a ferrous sulfate filter to remove impurities (NO₂, HONO, and so on) before
203 being injected into the detection cell. The NO concentration ($\sim 1.6 \times 10^{12} \text{ cm}^{-3}$)
204 corresponding to a conversion efficiency of ~15% was selected to avoid RO₂→HO₂
205 interference (especially from RO₂ radicals derived from long-chain alkanes (C ≥ 3),
206 alkenes, and aromatic hydrocarbons). Previous study denoted that the percentage
207 interference from alkene-derived RO₂ under these operating conditions was no more
208 than 5% (Wang et al., 2021).

209
210 A standard HO_x radical source was used to complete the calibration of the
211 detection sensitivity (Wang et al., 2020). The radical source is based on the
212 simultaneous photolysis of H₂O/O₂ by a 185 nm mercury lamp. Humidified air flow is
213 introduced to produce equal amounts of OH and HO₂ radicals after passing the
214 photolysis region. The flow remained in a laminar condition with a maximum flow
215 rate of 20 SLM (standard liters per minute). As the luminous flux in photolysis region
216 is difficult to accurately measure, the linearly correlation between ozone concentration

217 and 185 nm light flux was established. Ozone concentration in the flow tube was
218 measured by a home-made Cavity Ring Down Spectrometer (CRDS, and the
219 detection limit is 15 ppt@30 s, 1 σ). Mercury lamp intensity is adjusted to establish.
220 The instrument was calibrated every 1 or 2 days (except for shutdown during rainy
221 periods), and the sensitivity used for the data processing was an average of all of the
222 calibration results. In the YMK campaign, the humidity varied between 40 – 80% (Fig.
223 S3). In order to test different atmospheric conditions, both low (~40%) and high
224 (~70%) levels of water vapor were selected to produce OH and HO₂ radicals for
225 calibration, and the corresponding HOx concentration obtained from the standard
226 source was $1.0 \times 10^9 \text{ cm}^{-3}$ and $1.8 \times 10^9 \text{ cm}^{-3}$, respectively (Zhang et al., 2022b).

227 ~~___ A standard HOx radical source based on the simultaneous photolysis of H₂O/O₂~~
228 ~~by a 185 nm mercury lamp was used to complete the calibration of the detection~~
229 ~~sensitivity (Wang et al., 2020). ~~{[Renzi, 2016 #3450]}~~ During the observation~~
230 ~~campaign, the instrument was calibrated every 1 or 2 days (except for shutdown~~
231 ~~during rainy periods), and the sensitivity used for the data processing was an average~~
232 ~~of all of the calibration results. Considering the system uncertainty and calibration~~
233 ~~uncertainty ~~system error and calibration error~~, the detection limits of the OH and HO₂~~
234 ~~radicals were $3.3 \times 10^5 \text{ cm}^{-3}$ and $1.1 \times 10^6 \text{ cm}^{-3}$ (60 s, 1 σ), respectively, ~~at~~ At~~
235 ~~a typical laser power of 15 mW, and the measurement accuracy for OH and HO₂~~
236 ~~measurement errors ~~were~~ as 13% and 17%, respectively.~~

237 **2.2.2 Supporting measurements**

238 In addition to measuring the HOx radicals, an extensive suite of relevant species
239 was also measured close to the LIF instrument to improve the analysis of the radical
240 photochemistry. Detailed information about the measurement instrument is presented
241 in Table ~~S1~~S2, including the meteorological parameters (wind speed (WS), wind
242 direction (WD), temperature (T), relative humidity (RH), pressure (P), and solar
243 radiation (J-values)), ~~conventional and chemical parameters pollutants~~ (ozone (O₃),
244 ~~carbon monoxide carbonic oxide~~ (CO), ~~and~~ sulfur dioxide (SO₂), ~~), secondary~~
245 ~~pollution precursors~~ (HONO, NO, NO₂, HCHO, ~~and~~ NMHCs), and ~~destruction~~

246 ~~products~~ (particulate matter (PM_{2.5})). HONO measurement was conducted using a
247 commercial Long-Path Absorption Photometer (LOPAP). The LOPAP method utilizes
248 two absorption tubes in series for differential correction, which effectively eliminates
249 the influence of known interfering substances such as NO₂ and N₂O₅, offering an
250 advantage over traditional wet chemistry methods. Zero air measurements were taken
251 every 8 hours for a duration of 20 minutes to correct for instrument baseline
252 fluctuations. This method has been extensively tested for its suitability in detecting
253 HONO in complex atmospheric conditions, as demonstrated in previous studies by
254 (Yang et al., 2022b; Yang et al., 2021b; Wang et al., 2023), (Yang et al., 2022b; Yang et
255 al., 2021b; Zhu et al., 2020) Eight measured photolysis rates (j(NO₂), j(H₂O₂),
256 j(HCHO), j(HONO), j(NO₂), j(NO₃), j(O₁D)) were used as model constraints. –In
257 addition to HCHO, other volatile organic compounds (VOCs) were detected using a
258 gas chromatograph coupled with a flame ionization detector and mass spectrometer
259 (GC-FID-MS). Ninety-nine types of VOCs, including C₂–C₁₁ alkanes, C₂–C₆ alkenes,
260 C₆–C₁₀ aromatics, halohydrocarbons, and some oxygenated VOCs (OVOCs), were
261 observed using the GC-FID-MS at a 1-h time interval. Only isoprene was considered
262 as a representative of biogenic VOCs (BVOCs). All of the instruments were located
263 close to the roof of ~~the fourth floor~~ the monitoring building, nearly 12 m above the
264 ground to ensure that all of the pollutants were located in a homogeneous air mass.

265 **2.3 Model description**

266 A 0-D chemical box model incorporating a condensed mechanism, the regional
267 atmospheric chemistry mechanism version 2-Leuven isoprene mechanism (RACM2-
268 LIM1), was used to simulate the radical concentrations and the generation of ~~radical-~~
269 ~~related secondary pollution~~ ozone (Stockwell et al., 1997; Griffith et al., 2013; Tan et
270 al., 2017). The meteorological parameters, ~~conventional~~ pollutants, and precursor
271 concentrations mentioned in Section 2.2.2 were input into the model as boundary
272 conditions. All of the constraints were unified to a temporal resolution of 15 min
273 through averaging or linear interpolation. The overall average during the observations
274 was substituted for large areas of missing data due to instrument maintenance or

275 failure. Three days of data were entered in advance as the spin-up period, and a
 276 synchronized time-dependent dataset was eventually generated. The hydrogen (H₂)
 277 and methane (CH₄) concentrations were set to fixed values of 550 ppb and 1900 ppb,
 278 respectively. The physical losses of species due to processes such as deposition,
 279 convection, and advection were approximately replaced by an 18 h atmospheric
 280 lifetime, corresponding to first order loss rate of ~1.5 cm/s (by assuming a boundary
 281 layer height of about 1 km). The sensitivity analysis shows that when the lifetime
 282 changes within 8 – 24 hours, the values differed less than 5% for both OH, HO₂, k_{OH}
 283 (Fig. S4). According to the measurement accuracy, the simulation accuracy of the
 284 model for the OH and HO₂ radicals was 50% (Zhang et al., 2022a).

285 In addition, another steady-state calculation method (PSS) can also be used to
 286 estimate the concentrations of OH and HO₂ radicals (Eq. (1)(2), (Woodward-Massey
 287 et al., 2022b; Slater et al., 2020)). Since the k_{OH} and RO₂ concentrations were not
 288 obtained in this observation, simulated values are used as substitutes. Other radical
 289 and reactive intermediates are actual values that measured from the instruments in
 290 Table S2.

$$291 \quad [OH]_{PSS} = \frac{j_{HONO}[HONO] + \varphi_{OH}j(O^1D)[O_3] + k_{HO_2+NO}[NO][HO_2]}{k_{OH}} \quad (1)$$

$$292 \quad [HO_2]_{PSS} = \frac{k_{CO+OH}[CO][OH] + j_{HCHO}[HCHO] + k_{RO_2+NO}[NO][RO_2]}{k_{HO_2+NO}[NO]} \quad (2)$$

293
 294 Considering the environmental characteristics of the MBL, the gas-phase
 295 mechanisms for bromine (Br₂) and iodine (I) were introduced into the base model to
 296 diagnose the impacts of the reactive bromine chemistry ~~at the field site~~. The details of
 297 the mechanisms involved are listed in Tables S2-S3 and S3S4. The halogen species
 298 were not available in the YMK site, so the typical levels of BrO and IO₂
 299 ~~concentration during the same season in MBL site at a coastal site in the Pearl River~~
 300 Delta was used as a reference value (average daytime concentration ~~of of ~5 ppt~~
 301 ~~ppt at a coastal ground site in Hong Kong, China)~~ (Xia et al., 2022; Bloss et al., 2010;
 302 Whalley et al., 2010).

303 The heterogeneous uptake of HO₂ is considered to play an important role in the

304 MBL region (Whalley et al., 2010; Zou et al., 2022; Woodward-Massey et al., 2022b).
305 In order to assess the impact of HO₂ uptake on HO_x radical chemistry, we
306 incorporated HO₂ uptake reaction into the base model (Eq. (3) - (5)).



$$k_{HO_2+uptake} = \frac{\gamma \times ASA \times v_{HO_2}}{k_{HO_2+NO}[NO]} \quad (4)$$

$$v_{HO_2} = \sqrt{\frac{8 \times R \times T}{0.033 \times \Pi}} \quad (5)$$

310 Here, ASA represents the aerosol surface area [$\mu\text{m}^2 \text{cm}^{-3}$], which can be estimated
311 as 20 times the PM_{2.5} concentration [$\mu\text{g}/\text{cm}^3$]. v_{HO_2} [cm^{-1}] can be calculated using Eq.
312 (5), where T and R represent the temperature and gas constant, respectively. The
313 heterogeneous uptake coefficient (γ) for HO₂ usually has high uncertainty, with typical
314 values ranging from 0 to 1 (Song et al., 2021). In this study, we set γ to 0.08 to
315 evaluate the influence of HO₂ uptake on radical concentrations.

317 **3 Results**

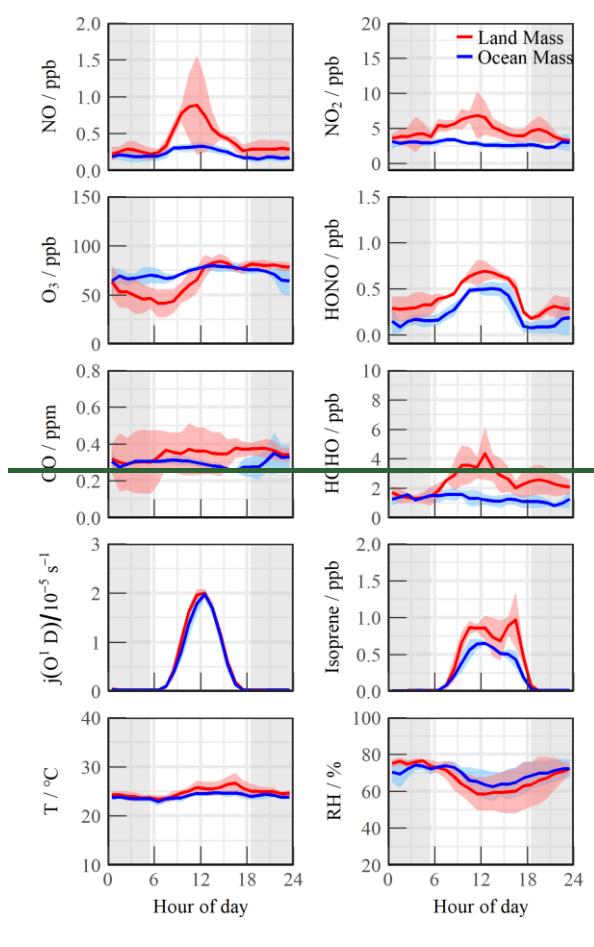
318 **3.1 Meteorological and chemical parameters**

319 **3.1.1 Data overview**

320 Fig. S1-S3 presents the time series of the main meteorological parameters and
321 pollutants during the observation period at the YMK site. Except for on 2 days,
322 October 26 and 28, the meteorological characteristics of the other days were generally
323 stable. The daily maximum T, RH, and J-values did not vary significantly. The
324 suitable temperature (20–30°C) and humidity (50–80%) conditions promoted the
325 stable oxidation of the diurnal photochemistry. The peak $j(\text{O}^1\text{D})$ value was
326 approximately $2.0 \times 10^{-5} \text{ s}^{-1}$, exhibiting the typical characteristics of intense light
327 radiation in autumn in the Pearl River Delta region (Yang et al., 2022b; Tan et al.,
328 2022).

329
330 As typical marine air components, the concentrations of NO_x, CO, PM_{2.5}, and

331 other pollutants were lower than those detected in other observation campaigns in
332 both urban and suburban areas in the Pearl River Delta region (Tan et al., 2019b; Lu et
333 al., 2012; Yang et al., 2022a). Serval observation campaigns have discovered the
334 relationship between wind direction and radical chemistry (Lu et al., 2012; Fuchs et
335 al., 2017; Niu et al., 2022). Although there was no apparent wind speed condition, the
336 dominant air mass still influenced the pollutant concentrations due to the particularity
337 of the marine site.



338

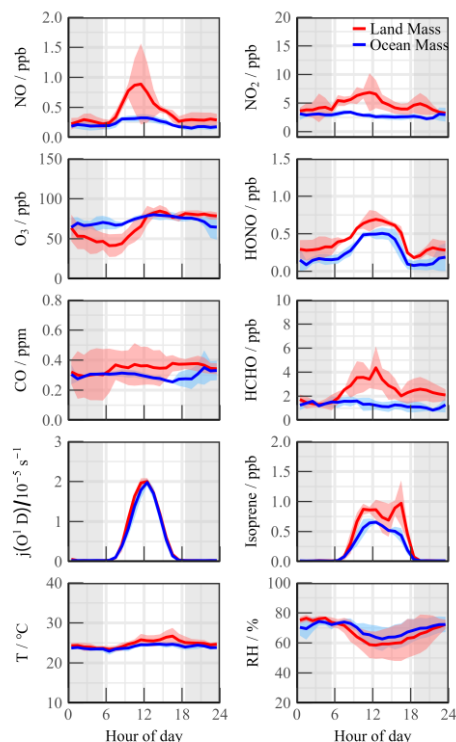


Fig. 2. Mean diurnal profiles of measured trace gases parameters during Land mass and Ocean mass episodes. The coloured shadows denote the 25 and 75% percentiles. The grey areas denote nighttime.

During the OCM period, the NO_x and HCHO concentrations exhibited relatively clean characteristics that were consistent with those previously observations in open ocean (RHAMBLe, SOS, CHABLIS and ALBATROSS, Table 1). Isoprene, a representative BVOC, achieved a diurnal concentration of 0.58 ± 0.06 ppb, indicated slightly local emissions could have impacted the concentrations of the precursor species even in OCM sector. The ozone concentration in the YMK site was always at the critical value of the updated Class I standard (GB3095-2012, average hourly O₃ of 81 ppb at 25°C and 1013 kPa). The occurrence of fewer emissions reduced the titration effect, resulting in the ozone exhibiting no apparent diurnal trend on some of the dates and a high background value at night (78.1 ± 7.6 ppb).

As a coastal site, chemical conditions could be influenced by local land emissions depending on the wind direction. Compared with the OCM period, the meteorological conditions (T, RH, and J-values) changed slightly during the LAM episode, but the pollutants were accumulated due to the transport of the plume from the northern cities (Fig. 2). The CO and PM_{2.5} concentrations exhibited good

358 consistency and even mild pollution features ((0.36 ± 0.12 ppm) and (37.70 ± 7.91
359 µg/m³), respectively), reflecting the influence of human activities. Both NO and NO₂
360 peaked at around 10:00, exhibiting prominent pollution characteristics. HONO
361 exhibited a distribution with high daytime (0.66 ± 0.08 ppb) and low nighttime (0.33
362 ± 0.09 ppb) concentrations. This unique distribution of HONO has been observed in
363 remote environments in several previous observation campaigns (Jiang et al., 2022;
364 Crilley et al., 2021). High HONO concentration in the daytime will affect the
365 chemical composition of the atmosphere and the secondary pollution generation. The
366 PM_{2.5} and CO concentrations exhibited good consistency and even mild pollution
367 features on some dates, reflecting the influence of human activities. Contrary to the
368 conventional belief that marine ozone is a global background setting, the ozone
369 concentration in the YMK site was always at the critical value of the updated Class I
370 standard (GB3095-2012, average hourly O₃ of 81 ppb at 25°C and 1013 kPa). The
371 occurrence of fewer emissions reduced the titration effect, resulting in the ozone
372 exhibiting no apparent diurnal trend on some of the dates and a high background
373 value at night (67.3 ± 7.6 ppb). The NO_x concentrations also maintained typically low
374 levels on most dates. Serval observation campaigns have discovered the relationship
375 between wind direction and radical chemistry (Lu et al., 2012; Fuchs et al., 2017; Niu
376 et al., 2022). Although there was no apparent wind speed condition, the dominant air
377 mass still influenced the pollutant concentrations due to the particularity of the marine
378 site. During the OCM period, the NO_x and HCHO concentrations exhibited relatively
379 clean characteristics that were consistent with those previously reported (Table 1).
380 However, both the HONO and O₃ concentrations were twice as high as those of the
381 other components, and their daily average values (10:00–15:00) reached 0.48 ppb and
382 78.1 ppb, respectively. Compared with the OCM period, the meteorological
383 conditions (T, RH, and J values) changed greatly during the LAM episode. The
384 pollutants were accumulated due to the transport of the plume from the northern cities
385 (Fig. 2). Both NO and NO₂ peaked at around 10:00, exhibiting prominent pollution
386 characteristics. The diurnal peaks of the HONO and HCHO concentrations were much

387 higher than those of the Integrated Chemistry of Ozone in the Atmosphere (ICOZA)
 388 Project observations (a pollution period dominated by a southwest wind direction)
 389 (Woodward-Massey et al., 2022b). The HONO concentration was 6.8 times higher
 390 than when the wind direction was southwest in the ICOZA observations, while the
 391 HCHO concentration was 3.1 times higher. The abundance of oxidation precursors
 392 (HONO, HCHO, O₃, and NMHCs) reflected the unique atmospheric conditions in the
 393 marine environment in China, which originated from the complex atmospheric
 394 pollution.

396 ~~The NO_x concentrations also maintained typically low levels on most dates. The~~
 397 ~~daily maximum NMHC concentration peaked at 19.3 ± 3.0 ppb, and the maximum~~
 398 ~~value of ~40 ppb occurred on October 27. Local biological emissions significantly~~
 399 ~~affected the NMHC composition of the site, and isoprene, a representative BVOC,~~
 400 ~~achieved a noon maximum of 0.82 ± 0.16 ppb. Neither anthropogenic alkenes nor~~
 401 ~~aromatic hydrocarbons were abundant, and OVOCs accounted for approximately 50%~~
 402 ~~of the total. As a photochemical indicator, formaldehyde peaked at ~4 to ~8 ppb on~~
 403 ~~October 18, 19, and 27, suggesting a more vigorous oxidation process. HONO~~
 404 ~~exhibited a grooved distribution with high daytime (0.49 ± 0.097 ppb) and low~~
 405 ~~nighttime (0.20 ± 0.11 ppb) concentrations. This unique distribution of HONO has~~
 406 ~~been observed in remote environments in several previous observation campaigns~~
 407 ~~(Jiang et al., 2022; Crilley et al., 2021). An extremely high daytime HONO~~
 408 ~~concentration will significantly affect the chemical composition of the atmosphere~~
 409 ~~and the secondary pollution generation.~~

410 **Table 1.** Summary of radical concentrations and related species concentrations at MBL. All data are listed as the
 411 average in noontime (10:00~15:00).

Campaign	Location	Category	Date	OH (10 ⁶ cm ⁻³)	HO ₂ (10 ⁸ cm ⁻³)	HCHO (ppb)	HONO (ppb)	NO _x (ppb)	O ₃ (ppb)	Reference
WAOSE95	Weybourne, UK	<u>Coastal</u>	1995 (Jun)	5.0	-	1.50	0.10	<2.0	40.0	(Grenfell et al., 1999)
ALBATROSS	Atlantic Ocean	<u>Open ocean</u>	1996 (Oct-Nov)	7.0	-	0.50	-	-	25.0	(Brauers et al., 2001)
EASE96	Mace Head, Ireland	<u>Coastal</u>	1996 (Jul-Aug)	2.3	2.6	-	-	~1.0	45.0	(Carslaw et al., 1999)
EASE97	Mace Head, Ireland	<u>Coastal</u>	1997 (Apr-May)	1.8	1.0	0.70	-	0.95	46.0	(Creasey et al., 2002)

ORION ⁹⁹	Okinawa Island, Japan	<u>Coastal</u>	1999 (Aug)	4.0	4.3	-	0.20	6.3	23.0	(Kanaya et al., 2001)
RISOTO	Rishiri Island, Japan	<u>Coastal</u>	2000 (June)	7.4	3.1	-	-	0.45	-	(Kanaya et al., 2002)
RISFEX	Rishiri Island, Japan	<u>Coastal</u>	2003 (Aug)	2.7	1.5	-	-	0.2	28.0	(Qi et al., 2007)
<u>CHABLIS</u>	<u>Antarctica</u>	<u>Open ocean</u>	<u>2005 (Jan-Feb)</u>	<u>1.0</u>	<u>1.1</u>	<u>0.12</u>	<u>0.007</u>	<u>0.02</u>	<u>7.0</u>	(Bloss et al., 2010)
RHaMBLe	Cape Verde, Atlantic Ocean	<u>Open ocean</u>	2007 (May-Jun)	9.0	6.0	0.30	-	0.014	35.0	(Whalley et al., 2010)
SOS	Cape Verde, Atlantic Ocean	<u>Open ocean</u>	2009 (Jun; Sep)	9.0	4.0	1.9	-	0.050	40.0	(Carpenter et al., 2011)
CYPHEX	Cyprus, Mediterranean	<u>Coastal</u>	2014 (Jul)	5.8	6.3	~1.0	~0.080	<1.0	69.0	(Mallik et al., 2018)
ICOZA (NW-SE)	North Norfolk, UK	<u>Coastal</u>	2015 (Jul)	3.0	1.4	0.9	0.052	2.0	39.0	(Woodward-Massey et al., 2022b)
ICOZA (SW)	North Norfolk, UK	<u>Coastal</u>	2015 (Jul)	4.1	1.0	1.1	0.097	3.0	31.0	(Woodward-Massey et al., 2022b)
HT	Hok Tsui, China	<u>Coastal</u>	2020 (Oct-Nov)	4.9	-	1.0	0.15	~4.0	65.0	(Zou et al., 2022)
YMK (Land Mass)	Shenzhen, China	<u>Coastal</u>	2019 (Oct)	7.1	5.2	3.4	0.66	6.4	75.6	This work
YMK (Ocean Mass)	Shenzhen, China	<u>Coastal</u>	2019 (Oct)	4.5	4.9	1.2	0.48	3.0	78.1	This work

412

413

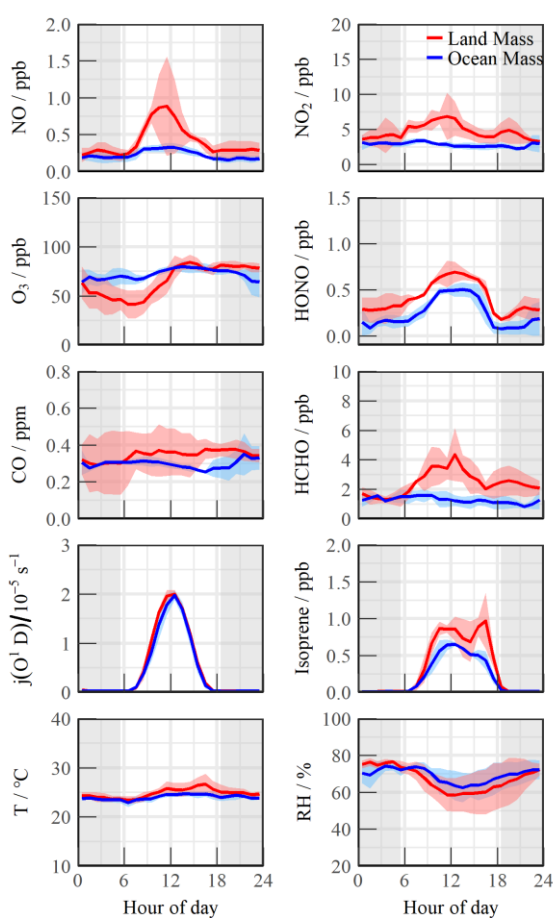
414 The detailed information for VOCs species during the YMK campaign has415 been added in the Table S5. The daily maximum NMHC concentration peaked at416 27.81 ± 9.91 ppb, and the maximum value of ~40 ppb occurred on October 27.417 Local biological emissions significantly affected the NMHC composition of the418 site, and isoprene achieved a noon maximum of 0.82 ± 0.16 ppb. Neither419 anthropogenic alkenes (2.21 ± 0.94 ppb) nor aromatic (1.31 ± 0.25 ppb)420 hydrocarbons were abundant, and OVOCs accounted for approximately 50% of421 the total. As a photochemical indicator, formaldehyde peaked at ~4 to ~8 ppb422 during the LAM episode, suggesting a more vigorous oxidation process. The423 HONO concentration was 6.8 times higher than the SW scenario in the ICOZA424 observation (a pollution period dominated by a southwest wind direction), while425 the HCHO concentration was 3.1 times higher. (Woodward-Massey et al., 2022b).

426 The abundance of oxidation precursors (HONO, HCHO, O₃, and NMHCs)
427 reflected the unique atmospheric conditions in the marine environment in China,
428 which originated from the complex atmospheric pollution.**3.1.2 Influences of**
429 **different air masses**

430 During the ~~YMK~~ observation campaign, the wind direction was mainly easterly
431 and southerly, and the wind speed was below 3 m/s. The conventional wind direction
432 is insufficient to reflect the air mass trajectory at a slightly higher altitude due to the
433 mountain-valley breeze (Niu et al., 2022). Using the hybrid single-particle Lagrangian
434 integrated trajectory (HYSPLIT) model, the 24 h backward trajectories on special
435 days were obtained (Fig. S2). In Fig. S2, the red, blue, and green trajectories represent
436 the results at altitudes of 100, 500, and 1000 m above ground level, respectively. Two
437 typical transportation pathways dominated the air parcels. One originated from the
438 northern megacities in the Pearl River Delta (defined as the land mass, LAM),
439 especially on October 18, 19, and 27. In contrast, a clean air mass from the east or
440 northeast was mainly transported to the observation site from the ocean (defined as
441 the ocean mass, OCM), with representative episodes on October 22, 25, and 26.

442 Serval observation campaigns have discovered the relationship between wind
443 direction and radical chemistry (Lu et al., 2012; Fuchs et al., 2017; Niu et al., 2022).
444 Although there was no apparent wind speed condition, the dominant air mass still
445 influenced the pollutant concentrations due to the particularity of the marine site.
446 During the OCM period, the NO_x and HCHO concentrations exhibited relatively
447 clean characteristics that were consistent with those previously reported (Table 1).
448 However, both the HONO and O₃ concentrations were twice as high as those of the
449 other components, and their daily average values (10:00–15:00) reached 0.48 ppb
450 and 78.1 ppb, respectively. Compared with the OCM period, the meteorological
451 conditions (T, RH, and J values) changed greatly during the LAM episode. The
452 pollutants were accumulated due to the transport of the plume from the northern
453 cities (Fig. 2). Both NO and NO₂ peaked at around 10:00, exhibiting prominent
454 pollution characteristics. The diurnal peaks of the HONO and HCHO

455 concentrations were much higher than those of the Integrated Chemistry of Ozone
 456 in the Atmosphere (ICOZA) Project observations (a pollution period dominated by
 457 a southwest wind direction) (Woodward-Massey et al., 2022b). The HONO
 458 concentration was 6.8 times higher than when the wind direction was southwest in
 459 the ICOZA observations, while the HCHO concentration was 3.1 times higher. The
 460 abundance of oxidation precursors (HONO, HCHO, O₃, and NMHCs) reflected the
 461 unique atmospheric conditions in the marine environment in China, which
 462 originated from the complex atmospheric pollution.

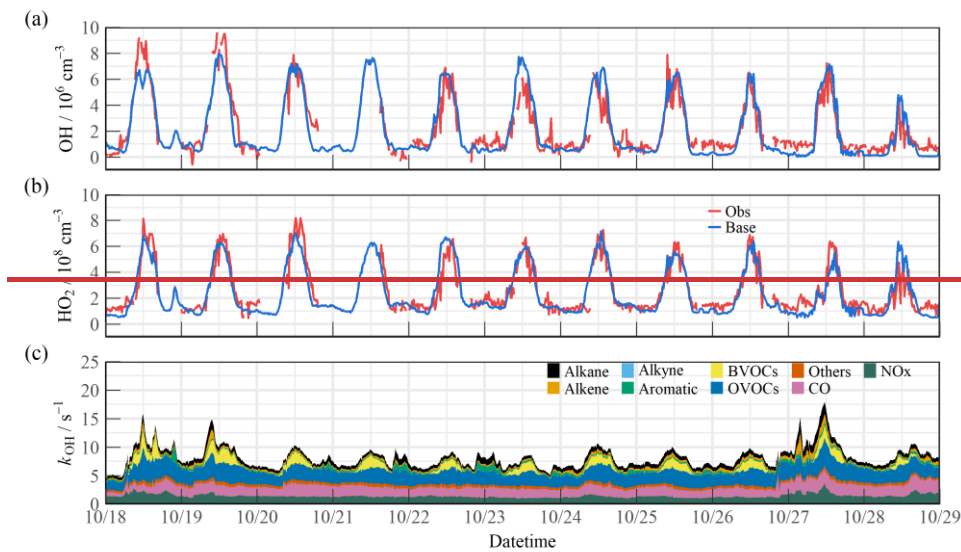


463 =
 464 **Fig. 2.** Mean diurnal profiles of measured trace gases parameters during Land mass and Ocean mass
 465 episodes. The coloured shadows denote the 25 and 75% percentiles. The grey areas denote nighttime.

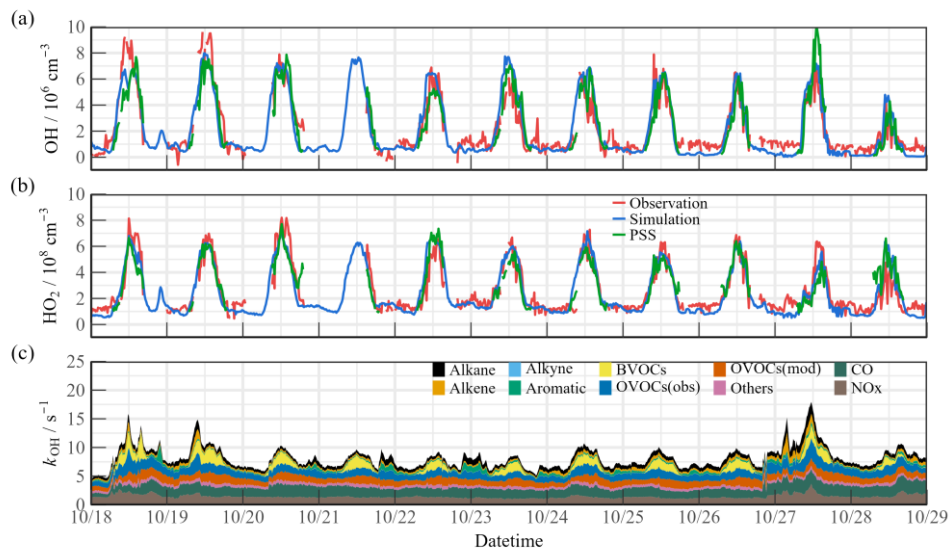
466 3.2 HOx radical concentrations and modeled OH reactivity

467 Fig. 3(a) and (b) shows the time series of the simulated and observed OH and
 468 HO₂ radical concentrations during the observation campaign. The time series of the
 469 simulated OH reactivity (k_{OH}) is presented in Fig. 3(c). The observed OH and HO₂

470 radicals exhibited significant diurnal trends. The ~~average~~-daily maximum OH and
471 HO₂ values were $(4.7\text{--}9.5) \times 10^6 \text{ cm}^{-3}$ and $(4.2\text{--}8.1) \times 10^8 \text{ cm}^{-3}$, respectively. The
472 peak k_{OH} value was commonly less than 10 s^{-1} . Due to human activities, the simulated
473 k_{OH} reached more than $\sim 15 \text{ s}^{-1}$ on some days. The radical concentrations and
474 reactivity exhibited similar trends, which differed from reports on urban and semi-
475 urban areas where inorganic species (NO_x and CO) were the dominant controllers of
476 k_{OH} (Zhang et al., 2022a; Tan et al., 2019b; Lou et al., 2010). The k_{OVOCs} was
477 separated into $k_{\text{OVOCs(Obs)}}$ and $k_{\text{OVOCs(Model)}}$ (Fig. 3(c)). Specifically, $k_{\text{OVOCs(Obs)}}$ includes
478 the observed species such as formaldehyde (HCHO), acetaldehyde (ACD), higher
479 aldehydes (ALD), acetone (ACT), ketones (KET), and oxidation products of isoprene
480 (MACR and MVK). The model-generated intermediates, such as glyoxal,
481 methylglyoxal, methylethyl ketone, and methanol, are categorized as $k_{\text{OVOCs(Model)}}$.
482 Approximately 50% of the total k_{OVOCs} are represented by unconstrained species
483 ($k_{\text{OVOCs(Model)}}$), which contribute a daily k_{OH} of 1.39 s^{-1} . Overall, the observed OH and
484 HO₂ concentrations were both well reproduced by the base model incorporating the
485 RACM2-LIM1 mechanism. The observed OH was underestimated only on the first
486 days, and a slight model overestimation happened on October 23&24. PSS calculation
487 showed good agreement with the base model, providing evidence of the balance of
488 radical internal consistency in the daytime. It should be noted that the OH reactivity
489 of unmeasured VOCs may be underestimated due to the lumped groups in RACM2
490 mechanism.



491



492

493

494

Fig. 3. Timeseries of the observed and modelled parameters for OH, HO₂ and *k*_{OH} during the observation period. (a) OH, (b) HO₂, (c) *k*_{OH}.

495

496

497

498

499

500

501

502

503

504

The air mass transport of the precursors induced photochemistry accumulation, which was then reflected in the changes in the oxidation progress. It is worth comparing the concentrations and reactivities of the radicals by classifying the predominant air mass (Fig. 4). During the OCM period, the observed OH and HO₂ radicals could be reflected by the base chemical mechanism, with daily averages of $4.5 \times 10^6 \text{ cm}^{-3}$ and $4.9 \times 10^8 \text{ cm}^{-3}$, respectively. Compared to other campaigns (Table 1), the observed maximum values were within reasonable ranges (OH: $2 - 9 \times 10^6 \text{ cm}^{-3}$; HO₂: $1 - 6 \times 10^8 \text{ cm}^{-3}$). Despite low NO_x levels during the OCM period, the HO₂ radical was not overestimated using the base model, which was dissimilar to many MBL observations (Bloss et al., 2010). However, both the OH and HO₂ radical

505 concentrations reached higher levels during the LAM-dominant period, indicating a
506 more active photochemical process (Section 4.1). The diel averages for the OH and
507 HO₂ radicals were $7.1 \times 10^6 \text{ cm}^{-3}$ and $5.2 \times 10^8 \text{ cm}^{-3}$, respectively, which were
508 notably higher than the levels reported in the ICOZA observations (Woodward-
509 Massey et al., 2022b). The base scenario underestimated both the OH and HO₂
510 concentrations between 10:00 and 15:00, and the observation-to-model ratio was
511 greater than 1.2. The calculated daily maximum total OH reactivity was 8.8 s^{-1} , and
512 nearly 70% of the reactivity was accounted for by the organic species, among which
513 the OVOCs were the largest contributor (30.6%). The anthropogenic alkanes, alkenes,
514 and aromatic hydrocarbons contributed less than 10% to the reactivity. Compared
515 with the OCM-dominant episode, the higher reactivity during the LAM period
516 indicated the occurrence of efficient recycling during the ROx (the sum of OH, HO₂,
517 and RO₂) propagation (12.4 s^{-1} vs. 8.8 s^{-1}). The higher contributions of the BVOCs
518 (only isoprene was considered, 15.6%) and OVOCs (30.2%) to the reactivity reflected
519 the diverse composition of the VOCs in the forest environment. Under enhanced
520 photochemistry, the calculated OH reactivity could be an underestimation of the total
521 OH reactivity, so a missing OH source may be masked. As a representative of the
522 OVOCs, HCHO reflects the photochemical level to a certain extent. As shown in Fig.
523 S5, a solid positive dependence between the OH_{obs-to-OH_{mod}} ratio and HCHO was
524 observed (the daytime data were restricted according to $j(\text{O}^1\text{D}) > 5 \times 10^{-6} \text{ s}^{-1}$). With
525 the increase of photochemical intensity, the ratio between the observed and simulated
526 OH radical showed an obvious mismatch. Obtaining the full magnitude of the radical-
527 related parameters is necessary to compensate for the discrepancy in the concentration
528 closure experiments.

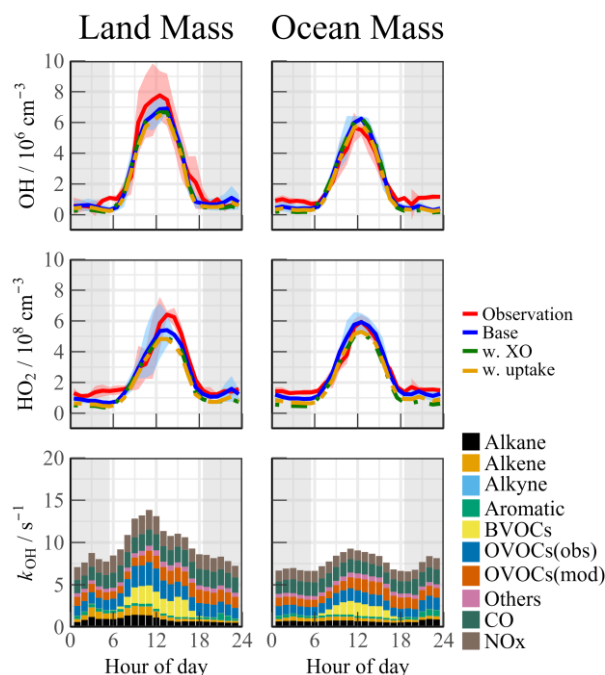


Fig. 4. Median diurnal profiles of the observed and modelled OH, HO₂, k_{OH} during LAM and OCM episodes. The coloured shadows for OH and HO₂ radicals denote the 25 and 75% percentiles. The grey areas denote nighttime.

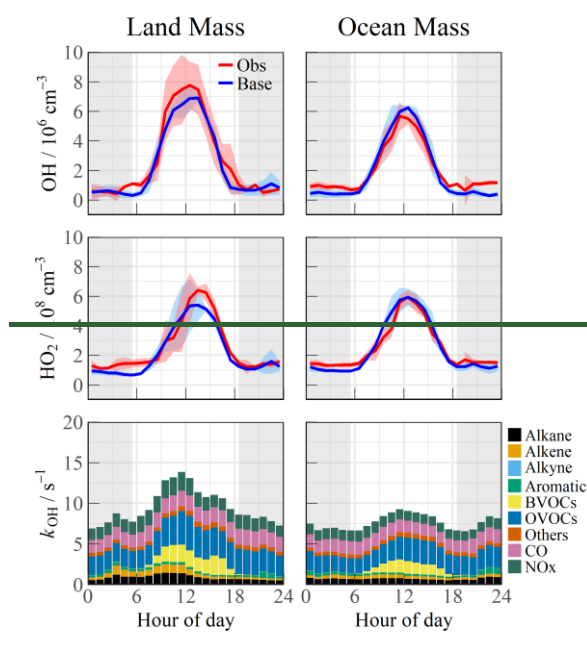
Halogen species have been recognized as potent oxidizers that can boost photochemistry (Xia et al., 2022; Peng et al., 2021). A sensitivity test was performed by imposing BrO and IO into the base model to diagnose the impact of the halogen chemistry on the troposphere chemistry. The concentration of BrO and IO is set to ~5 ppt, which is a typical level in MBL site (Xia et al., 2022; Bloss et al., 2010; Whalley et al., 2010). The details of the mechanisms involved are listed in Tables S3 and S4. In this scenario (Fig. 4, green line). The daytime concentration of HO₂ radical decreased by 8.5% and 13.3% during the LAM and OCM periods, respectively, compared to the base model. However, there was no significant change in the concentration of OH radicals (<3%). Traditionally, it is believed that the inclusion of halogen chemistry leads to higher modeled OH concentrations and lower modeled HO₂ concentrations. Therefore, the lack of an increase in OH concentration with the introduction of the halogen mechanism at the YMK site calls for further investigation (Fig. S6). By modifying the NO concentration in different levels (Scenario 1: [NO] × 150%, Scenario 2: base, Scenario 3: [NO] × 20%, Scenario 4: [NO] × 10%), the response of HO_x radicals to the halogen mechanism varied under different NO levels. As the

549 constrained NO increased from 30 ppt to 500 ppt, the reduction in HO₂ radicals due to
550 the Br and I mechanisms ranged between 10% and 20%. At elevated NO_x levels,
551 reactions between halogen radicals and NO_x occurred, inhibiting the formation of OH
552 radicals. In Scenario 1, the OH concentration even decreased by 3.5% when
553 introducing the halogen mechanism. When NO concentration was constrained around
554 30 ppt (Scenario 4), similar to those obtained in RHaMBLe/CYPHEX campaigns, the
555 modelled OH concentration increased by 14.4%, while the HO₂ concentration
556 decreased by approximately 20.8% (Whalley et al., 2010; Bloss et al., 2010).
557 Therefore, the sensitivity of OH radicals to the halogen mechanism in the YMK
558 region is primarily limited by the local NO_x concentration level.

559 Although the modelled and measured HO₂ showed good agreement, the effect of
560 HO₂ heterogeneous processes on the chemistry of HO_x radicals is also worth
561 exploring. The inclusion of heterogeneous processes ($\gamma = 0.08$) did reduce the
562 modelled HO₂ concentration for ~10% during both LAM and OCM periods (Fig. 4,
563 yellow line). This reduced agreement between observation and simulation emphasizes
564 the presence of a missing HO₂ source in the base model.

565
566 The heterogeneous uptake pathway did not need to be further investigated due to
567 the low PM_{2.5} concentration during the OCM period ($< 25 \mu\text{g}/\text{m}^3$). However, both
568 the OH and HO₂ radical concentrations reached higher levels during the LAM-
569 dominant period, indicating a more active photochemical process. The diel averages
570 for the OH and HO₂ radicals were $7.1 \times 10^6 \text{ cm}^{-3}$ and $5.2 \times 10^8 \text{ cm}^{-3}$, respectively,
571 which were notably higher than the levels reported in the ICOZA observations
572 (Woodward-Massey et al., 2022b). The base model underestimated both the OH and
573 HO₂ concentrations between 10:00 and 15:00, and the observation to model ratio was
574 greater than 1.2. Compared with the OCM-dominant episode, the higher reactivity
575 during the LAM period indicated the occurrence of efficient recycling during the RO_x
576 propagation (12.4 s^{-1} vs. 8.8 s^{-1}). The higher contributions of the BVOCs (only
577 isoprene was considered, 15.6%) and OVOCs (30.2%) to the reactivity reflected the

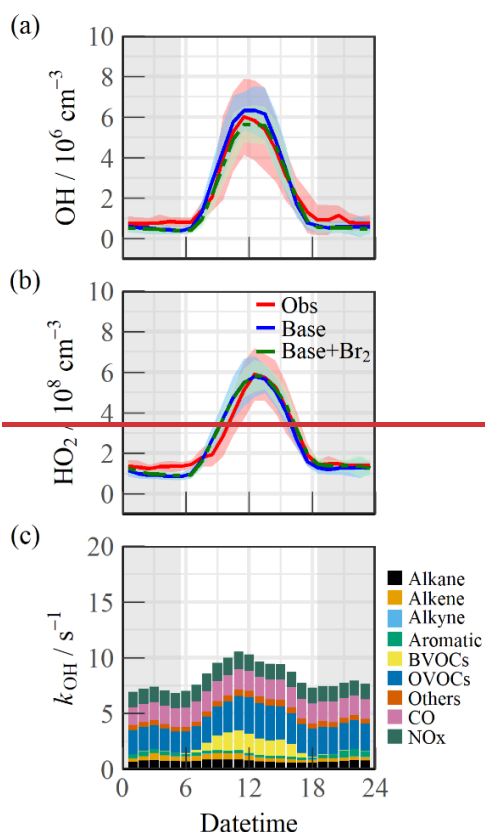
578 diverse composition of the VOCs in the forest environment. The more reactive
 579 atmosphere did not introduce a missing OH source in the afternoon, but radical
 580 cycling under enhanced photochemistry is worth discussing (Hofzumahaus et al.,
 581 2009). As a representative of the OVOCs, HCHO reflects the photochemical level to a
 582 certain extent. As shown in Fig. S3, a solid positive dependence between the OHobs-
 583 to-OHmod ratio and HCHO was observed (the daytime data were restricted according
 584 to $j(\text{O1D}) > 5 \times 10^{-6} \text{ s}^{-1}$). Considering the essential contributions of the OVOCs and
 585 BVOCs during ROx recycling, the other unmeasured species (mono-terpenes and
 586 reactive halogens) involved in the oxidation cycle were responsible for the elevated
 587 photochemistry. Obtaining the full magnitude of the radical-related parameters is
 588 necessary to compensate for the discrepancy in the concentration closure experiments.



589
 590 Fig. 4. Median diurnal profiles of the observed and modelled OH, HO₂, k_{OH} during LAM and OCM episodes.
 591 The coloured shadows for OH and HO₂ radicals denote the 25 and 75% percentiles. The grey areas denote
 592 nighttime.

593 The OH and HO₂ concentrations were calculated using a base model
 594 incorporating the RACM2 LIM1 mechanism. Overall, the observed OH and HO₂
 595 concentration data were both well reproduced by the base model (Fig. 4(a) (b)). The
 596 base model slightly overestimated the OH radical, suggesting that a radical removal
 597 pathway was missing. Halogen species have been recognized as potent oxidizers that
 598 can boost photochemistry (Xia et al., 2022; Peng et al., 2021). A sensitivity test was

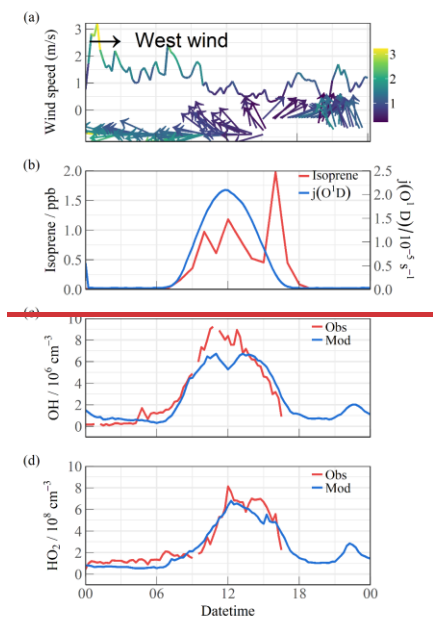
599 performed by imposing ~3 ppt Br₂, a typical mixing ratio reported for a coastal site in
 600 the Pearl River Delta, into the base model to diagnose the impact of the halogen
 601 chemistry on the troposphere chemistry (Xia et al., 2022). The details of the
 602 mechanisms involved are listed in Tables S2 and S3. In this scenario (Fig. 4(a) (b),
 603 green line), the simulated OH was 11.6% lower than in the base model, and no
 604 significant effect on the HO₂ radical was identified. The daily maximum calculated
 605 total OH reactivity was 9.9 s⁻¹ (Fig. 4(c)). Regarding the contributions of the
 606 inorganic species, the contributions of CO and NO_x were close at 18.0% and 14.8%,
 607 respectively. Nearly 70% of the reactivity was accounted for by the organic species,
 608 among which the OVOCs were the largest contributor (30.6%). The anthropogenic
 609 alkanes, alkenes, and aromatic hydrocarbons contributed less than 10% to the
 610 reactivity in the marine environment. The BVOCs emitted by the surrounding forest
 611 could not be ignored, accounting for 15.7%.



612 —
 613 **Fig. 4.** Median diurnal profiles of the observed and modelled parameters for OH, HO₂ and *k*_{OH} during the
 614 observation period. (a) OH, (b) HO₂, (c) *k*_{OH}.

615 The regional transport of radicals was generally impossible due to their short
 616 lifetimes. However, the air mass transport of the precursors increase the RO_x primary

617 sources. Under the linkage of NO concentration, this leads to accelerated cycling
 618 efficiency of the radicals, promoting the accumulation of photochemical products.
 619 The effects can be seen directly in the changes to the oxidation level. Isoprene is
 620 discussed as an example. The prevailing wind direction experienced a series of
 621 southerly easterly shifts from 8:00 to 18:00 on October 18 (Fig. 5(a)). The growth and
 622 decline of the isoprene concentration were highly correlated with the changes in the
 623 wind direction (Fig. 5(b)), and the maximum concentration (2.1 ppb) occurred at
 624 17:00 under the southwest wind. Correspondingly, the sensitive LIF instrument
 625 captured the decrease in the concentration at noon. The base model simulated the
 626 fluctuations in the OH concentration, but the solar radiation did not vary, indicating
 627 that the change in the precursor accelerated the instantaneous $\text{OH} \rightarrow \text{HO}_2$ propagation
 628 (Fig. 5(c)). In addition, the evolution of the air mass composition inhibited the
 629 conversion of HO_2 to OH and maintained the high HO_2 level during the afternoon
 630 (Fig. 5(d)).

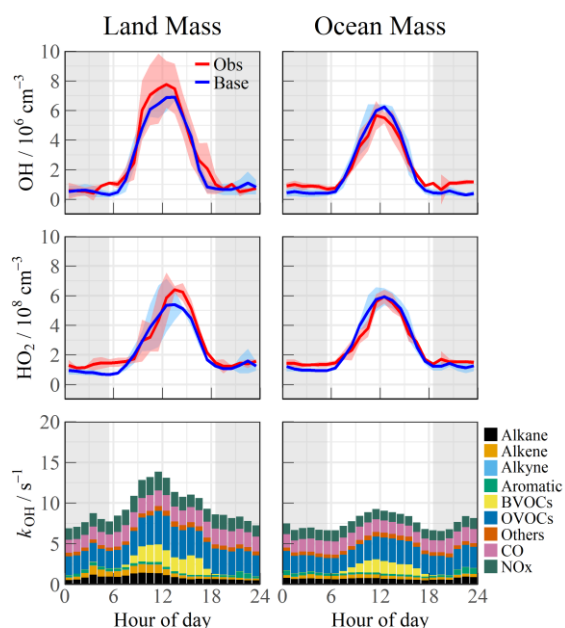


631 -
 632 **Fig. 5.** Median diurnal profiles of the observed and modelled parameters during a
 633 typical case of rapid wind direction change on October 18. (a) Wind direction and speed, (b)
 634 Isoprene concentration and solar radiation ($j(\text{O}^+\text{D})$), (c) The observed and modelled OH
 635 concentration, (d) The observed and modelled HO_2 concentration.

636 ~~Therefore, it is worth comparing the concentrations and reactivities of the~~

637 ~~radicals by classifying the predominant air mass (Fig. 6). During the OCM period,~~
638 ~~the observed OH and HO₂ radicals could be reflected by the base chemical~~
639 ~~mechanism, with daily averages of $4.5 \times 10^6 \text{ cm}^{-3}$ and $4.9 \times 10^8 \text{ cm}^{-3}$, respectively.~~
640 ~~Compared to other campaigns (Table 1), the observed maximum values were within~~
641 ~~reasonable ranges (OH: $2.9 \times 10^6 \text{ cm}^{-3}$; HO₂: $1.6 \times 10^8 \text{ cm}^{-3}$). Despite low NO_x~~
642 ~~levels during the OCM period, the HO₂ radical was not overestimated using the~~
643 ~~base model, which was dissimilar to many MBL observations. The heterogeneous~~
644 ~~uptake pathway did not need to be further investigated due to the low PM_{2.5}~~
645 ~~concentration during the OCM period ($< 25 \mu\text{g}/\text{m}^3$). However, both the OH and~~
646 ~~HO₂ radical concentrations reached higher levels during the LAM dominant period,~~
647 ~~indicating a more active photochemical process. The diel averages for the OH and~~
648 ~~HO₂ radicals were $7.1 \times 10^6 \text{ cm}^{-3}$ and $5.2 \times 10^8 \text{ cm}^{-3}$, respectively, which were~~
649 ~~notably higher than the levels reported in the ICOZA observations (Woodward-~~
650 ~~Massey et al., 2022b). The base model underestimated both the OH and HO₂~~
651 ~~concentrations between 10:00 and 15:00, and the observation to model ratio was~~
652 ~~greater than 1.2. Compared with the OCM dominant episode, the higher reactivity~~
653 ~~during the LAM period indicated the occurrence of efficient recycling during the~~
654 ~~RO_x propagation (12.4 s^{-1} vs. 8.8 s^{-1}). The higher contributions of the BVOCs~~
655 ~~(only isoprene was considered, 15.6%) and OVOCs (30.2%) to the reactivity~~
656 ~~reflected the diverse composition of the VOCs in the forest environment. The more~~
657 ~~reactive atmosphere did not introduce a missing OH source in the afternoon, but~~
658 ~~radical cycling under enhanced photochemistry is worth discussing (Hofzumahaus~~
659 ~~et al., 2009). As a representative of the OVOCs, HCHO reflects the photochemical~~
660 ~~level to a certain extent. As shown in Fig. S3, a solid positive dependence between~~
661 ~~the OH_{obs} to OH_{mod} ratio and HCHO was observed (the daytime data were~~
662 ~~restricted according to $j(\text{O}^1\text{D}) > 5 \times 10^{-6} \text{ s}^{-1}$). Considering the essential~~
663 ~~contributions of the OVOCs and BVOCs during RO_x recycling, the other~~
664 ~~unmeasured species (mono terpenes and reactive halogens) involved in the~~
665 ~~oxidation cycle were responsible for the elevated photochemistry. Obtaining the full~~

666 ~~magnitude of the radical related parameters is necessary to compensate for the~~
 667 ~~discrepancy in the concentration closure experiments.~~



668
 669 ~~Fig. 6. Median diurnal profiles of the observed and modelled OH, HO₂, k_{OH} during LAM~~
 670 ~~and OCM episodes. The coloured shadows for OH and HO₂ radicals denote the 25 and 75%~~
 671 ~~percentiles. The grey areas denote nighttime.~~

672 4 Discussion

673 4.1 Experimental radical budget balance

674 4.1.1 OH radical

675 A process-oriented experiment was conducted to investigate the photochemistry
 676 progress from a budget balance perspective (Woodward-Massey et al., 2022a; Tan et
 677 al., 2019b; Yang et al., 2021a). The OH was in a photostationary steady state due to its
 678 short lifetime. The total OH removal rate was directly quantified from the union of the
 679 OH concentration and the reactivity (R-Eq.(16)):

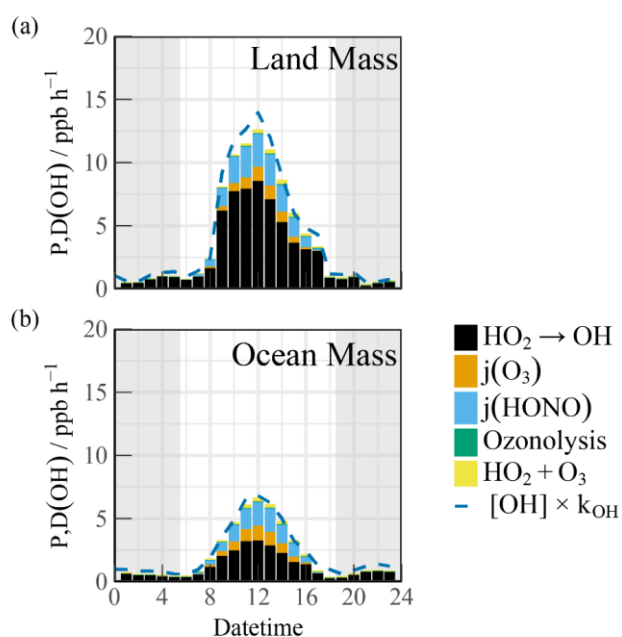
$$680 \quad D(OH) = [OH] \times k_{OH}. \quad (16)$$

681 The total production rate of the OH radical was the sum of the primary sources
 682 (O₃/HONO photolysis and ozonolysis reactions) and secondary sources (HO₂ + NO)
 683 (Eq.(7)R-(2)):

$$\begin{aligned}
P(OH) = & j_{HONO}[HONO] + \varphi_{OH}j(O^1D)[O_3] + \Sigma i \{ \varphi_{OH}^i k_{Alkenes+O_3}^i [Alkenes][O_3] \} \\
& + (k_{HO_2+NO}[NO] \\
& + k_{HO_2+O_3}[O_3])[HO_2]. \tag{27}
\end{aligned}$$

Here, φ_{OH} and φ_{OH}^i represent the OH yields in the O_3 photolysis and alkene ozonolysis processes, respectively.

The diel profiles of the experimental OH budget during the LAM and OCM periods are shown in Fig. 75. Both the observed OH and HO_2 radicals were introduced into the budget calculations. ~~Because k_{OH} was not measured during the observation experiment, the simulated value was used to analyze the removal rate. Therefore, $D(OH)$ should be considered a lower limit as it uses calculated rather than measured k_{OH} (Yang et al., 2022a).~~ Because k_{OH} was not measured during the observation experiment, the simulated value was used to analyze the removal rate. Therefore, $D(OH)$ should be considered a lower limit as it uses calculated rather than measured k_{OH} (Yang et al., 2022a). During the OCM period, the $HO_2 + NO$ reaction accounted for ~50% of the OH yield. The maximum of 6.6 ppb/h occurred at around 12:00. The photolysis reactions could increase the daytime contributions of HONO and O_3 to 1.52 ppb/h and 0.84 ppb/h, respectively (10:00–15:00). The contribution of the non-photolytic radical source (ozonolysis reactions) was almost negligible.



702

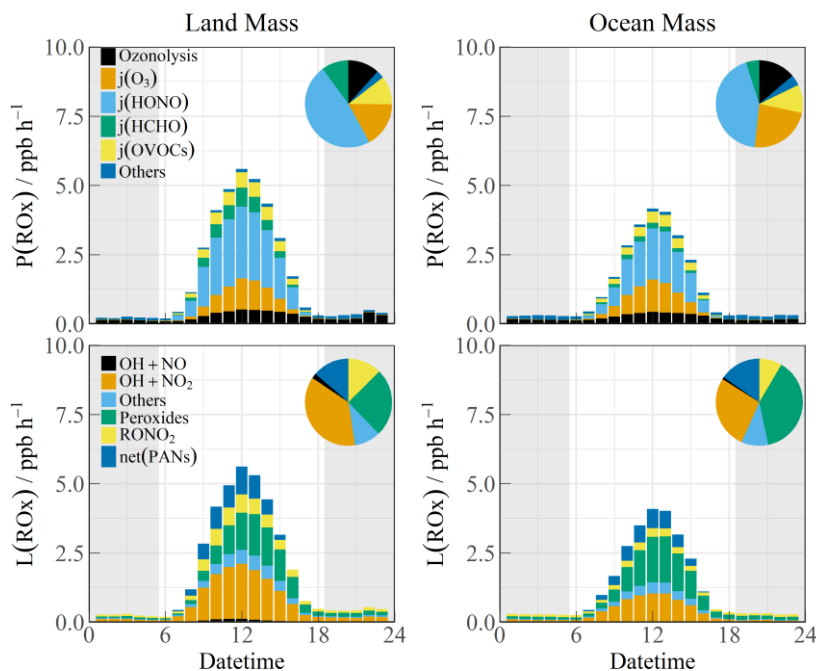
703 Fig. 75. The diurnal profiles of the experimental OH budget during (a) Land-massAM and (b) Ocean
704 massCM episodes. The blue line denotes the OH destruction rate($[OH] \times k_{OH}$). The grey areas denote nighttime.

705 Compared with other marine observations, the calculated OH generation rate was
706 approximately twice that reported in the ICOZA ~~Project~~ and five times that obtained
707 in the RHaMBLe ~~Project campaigns~~ (Woodward-Massey et al., 2022a; Whalley et al.,
708 2010). During the LAM period, the OH generation rate reached a maximum of 12.6
709 ppb/h, accompanied by a secondary source contribution of 67% (from the reaction
710 between HO₂ and NO) during the daytime, which was close to several observations
711 related to polluted plumes (Woodward-Massey et al., 2022a; Tan et al., 2019b; Lu et
712 al., 2012; Yang et al., 2022a). ~~When the simulated k_{OH} was introduced into the~~
713 ~~experimental budgets, tNo additional OH radical source was needed when the~~
714 ~~simulated k_{OH} was introduced into the experimental budgets.~~ The difference between
715 P(OH) and D(OH) was less than 2 ppb/h, ~~indicating the absence of a nontraditional~~
716 ~~OH recycling pathway (X mechanism) under low NO concentration conditions~~
717 ~~(Hofzumahaus et al., 2009).~~

718 4.1.2 Total ROx radicals

719 The budget analysis of the HO₂ and RO₂ radicals could not be performed well
720 due to the lack of RO₂ radical observation data. The diurnal profiles of the ROx
721 production (P(ROx)) and termination rate (L(ROx)) for the different air masses are
722 shown in Fig. 86. The P(ROx) could reach 3.36 ppb /h with an ocean plume. HONO
723 photolysis controlled nearly half of the primary sources (45.7%), and the daily
724 distribution was consistent with that of solar radiation. The ozone-related
725 contributions from photolysis and ozonolysis were approximately 46.6% (25.1% from
726 photolysis and 11.5% from ozonolysis+ 11.5%, respectively). The remaining
727 contribution was from the photolysis of carbonyls (HCHO and OVOCs) (15.0%). The
728 anthropogenic contribution to the radical chemistry was not ignorable, and the ROx
729 source in this observation was exponentially higher than that in other MBL
730 observations (Woodward-Massey et al., 2022a; Stone et al., 2012; Whalley et al.,
731 2010; Mallik et al., 2018). The P(ROx) of the LAM was close to that in Shenzhen (~4
732 ppb/h) but was significantly lower than that in Yufa (~7 ppb/h) and the BackGarden

733 (~11 ppb/h) (Tan et al., 2019b; Lu et al., 2012; Yang et al., 2022a). The reactions
 734 between ROx and NOx and self-combination were the main pathways of radical
 735 termination (~70%). The contribution of the formation of peroxynitrateperoxynitrite
 736 to the L(ROx) could not be ignored in the daytime.



737 **Fig. 86.** The diurnal profiles of ROx budget during Land mass and Ocean mass episodes. The pie chart
 738 denotes proportions in different parts during the daytime (10:00-15:00). The grey areas denote nighttime.
 739

740 The high daytime HONO concentrations observed at the YMK site is a notable
 741 phenomenon. Due to the high HONO concentration during the daytime, the photolysis
 742 reaction made daytime contributions of 1.52 ppb/h and 2.19 ppb/h during the OCM
 743 and LAM periods, respectively. As the only known gas-phase source, OH + NO
 744 accounted for a negligible proportion of the HONO production rate.~~As the only~~
 745 ~~known gas-phase source, OH + NO accounted for a negligible proportion of the~~
 746 ~~HONO loss.~~ Given the location of the site~~Considering the location of the YMK site,~~
 747 HONO from cruise ship emissions is a possible component of the primary
 748 anthropogenic source (Sun et al., 2020). Other active tropospheric HONO sources
 749 (heterogeneous reactions with NO₂ and $p(NO_3^-)$ photolysis) are worthy of
 750 consideration and significantly contribute to the atmospheric oxidation in the MBL
 751 area (Zhu et al., 2022; Crilley et al., 2021).

752 4.2 Local ozone production rate

753 Peroxy[†] radical chemistry is the essential photochemical source of tropospheric
 754 ozone (F(Ox), Eq.(8)R-(3)):

$$755 \quad F(O_x) = k_{HO_2+NO}[NO][HO_2] + \sum_i(1 - \alpha_i)k_{RO_2^i+NO}[NO]RO_2^i \quad (38)$$

756 NO reacts with HO₂ and RO₂ radicals to form NO₂, and then, photolysis occurs to
 757 form O₃ under solar radiation. NO₂ and ozone are the two sides of the oxidation
 758 reservoir. The effect of local emissions on the photodynamic equilibrium can be
 759 avoided by characterizing the photochemical production of the total oxidants (Tan et
 760 al., 2019b). α_i represents the side generation ratio of organic nitrate, which also
 761 affects the quantum yield of NO₂ (Tan et al., 2018). Ox is mainly photochemically
 762 removed through ozone photolysis, ozonolysis, radical chain propagation (OH/HO₂ +
 763 O₃), and chain termination (OH + NO₂) reactions in the troposphere (D(Ox), Eq.(9)R-
 764 (4)):

$$765 \quad D(O_x) = \varphi_{OH}j(O^1D)[O_3] + \sum_i \{k_{Alkenes+O_3}^i[Alkenes][O_3]\} + (k_{O_3+OH}[OH] +
 766 \quad k_{O_3+HO_2}[HO_2])[O_3] + k_{OH+NO_2}[OH][NO_2] \quad (94)$$

767 The net formation rate (P(Ox)) can be calculated by subtracting D(Ox) from F(Ox)
 768 (Eq.(10)):

$$769 \quad P(O_x) = F(O_x) - D(O_x) \quad (510)$$

770 The simulated RO₂ radical concentration was introduced into the F(Ox)
 771 calculation. The diurnal variations in the ozone generation in the different air masses
 772 are shown in Fig. 97. The contribution of the HO₂ radical to F(Ox) was approximately
 773 60%. The RO₂ radicals consisted of various types such as methyl peroxy[†] (MO₂),
 774 acetyl peroxy radicals (ACO₃/RCO₃), and other radicals derived from alkanes
 775 (ALKAP), alkenes (ALKEP), and isoprene (ISOP), which accounted for an additional
 776 40% of the F(Ox). On a daytime basis, the maximum F(Ox) reached 7.4 ppb/h at
 777 around 12:00 in the OCM period, while a persistent-high value (maximum of 12.5
 778 ppb/h at 10:00–14:00) occurred in the LAM period. A vast amount of Ox was
 779 consumed in the nitric acid (OH + NO₂) formation pathways, i.e., higher than the
 780 ozonolysis removal. The daily averaged ozone production rates were 5.52 and 2.76
 781 ppb/h during the LAM and OCM periods, respectively.

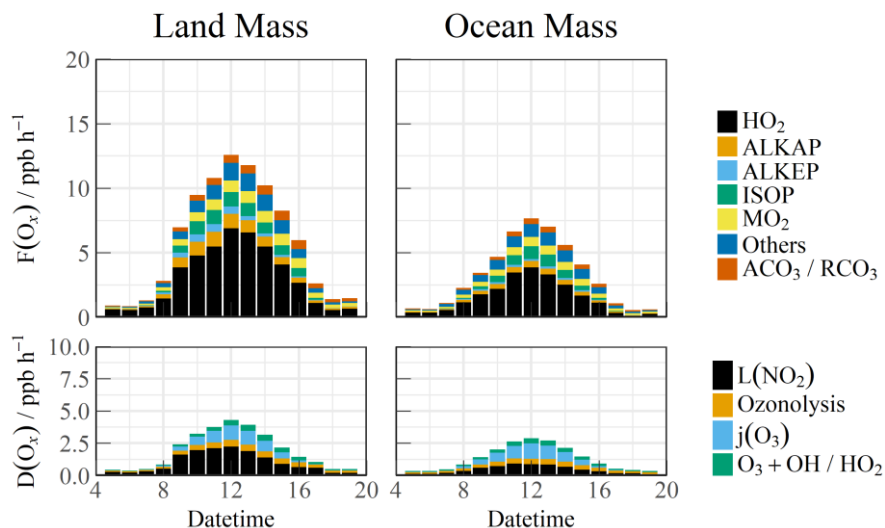
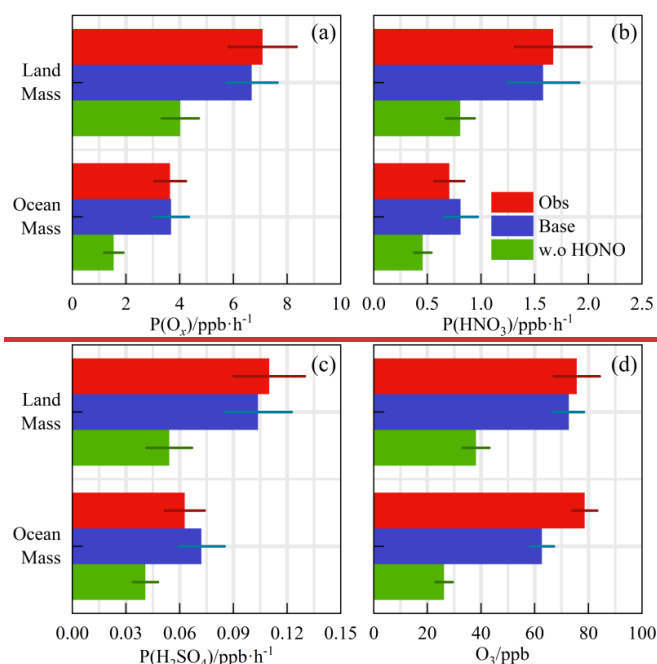


Fig. 97. The diurnal profiles of the speciation $F(O_x)$ and $D(O_x)$ during Land mass and Ocean mass episodes. The data were calculated by the measured OH and HO₂ and modelled RO₂ radicals.

4.3 Relationship between precursors and oxidation rates

Despite the low level of human activities, oxidation precursors have an extended lifetime in the stable atmosphere of coastal areas. Intensive photochemical reactions occur after the accumulation of precursors, resulting in local net ozone production comparable to that in the surrounding suburban environments (Zeren et al., 2022). Simultaneous observations of both urban and coastal settings in Shenzhen have indicated that the oxidation rates are comparable (Xia et al., 2021). The coupling of precursor transport and local photochemical processes in marine areas makes it meaningful to explore secondary pollution generation (Fig. 108(a), (b), and (c)). No obvious radical source was missing during the LAM and OCM periods, and the oxidation level was that expected from the base model. On a daytime basis, the mean diurnal profile of the $P(O_x)$ reached ~ 7 ppb/h in the LAM period, and the average nitric acid ($P(HNO_3)$) and sulfuric acid ($P(H_2SO_4)$) production rates were ~ 1.6 and ~ 0.11 ppb/h, respectively. The $P(HNO_3)$ production rate was similar to the average of observations in the Pearl River Delta region (~ 1.3 ppb/h), while that of the $P(H_2SO_4)$ was only half the average level (~ 0.24 ppb/h) (Lu et al., 2013; Tan et al., 2019b; Yang et al., 2022a). During the OCM period, the characteristics of the ocean air mass alleviated the photochemical process, and the production rates of the secondary

804 pollutants decreased by approximately half and were close to the average levels in
 805 winter (Ma et al., 2019).



806

807 **Fig. 10.** The calculated reaction rates based on the observed concentrations for Land mass and Ocean
 808 mass episodes (a) P(O_x), (b) P(HNO₃), (c) P(H₂SO₄). (d) The observed and modelled O₃ concentration with a
 809 first-order loss term. The deposition process was equivalent to a lifetime of 15 hours to all species. All the
 810 rates and concentration are averaged for the daytime period between 10:00 and 15:00.

811 Contrary to numerous ocean observations, in the YMK site, intensive oxidation
 812 was accompanied by a high diurnal HONO level (higher than 400 ppt) (Fig. 119). The
 813 ozone levels were consistent with the Grade I air quality standard and far exceeded
 814 the global background concentration (~40 ppb). Daytime photolysis reactions of
 815 HONO contributed 1.52 ppb/h and 2.19 ppb/h to P(RO_x) during the OCM and LAM
 816 periods, respectively, which were much higher than the values in several megacities
 817 during the photochemically polluted season (Tan et al., 2019a). Given the significance
 818 of HONO photolysis in driving atmospheric chemistry, a sensitivity test was
 819 conducted without constraints on HONO (i.e., w.o HONO) to specifically quantify the
 820 contribution of HONO-induced secondary pollution. Only the homogeneous reaction
 821 (OH + NO) participated in the formation of HONO in the default mode without
 822 HONO input (Liu et al., 2022b).

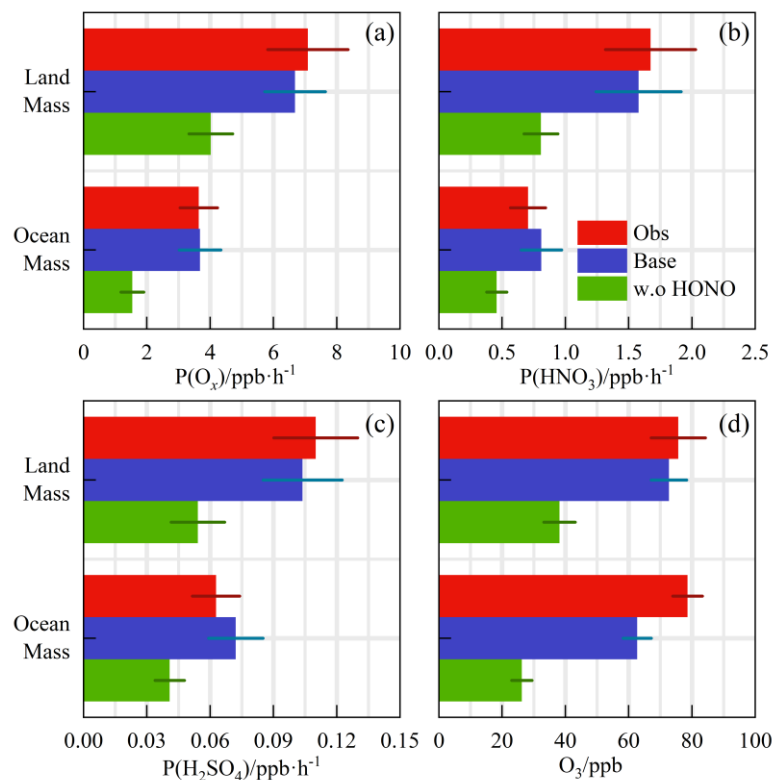


Fig. 8. The calculated reaction rates based on the observed concentrations for Land mass and Ocean mass episodes (a) $P(\text{Ox})$, (b) $P(\text{HNO}_3)$, (c) $P(\text{H}_2\text{SO}_4)$. (d) The observed and modelled O_3 concentration with a first-order loss term. The deposition process was equivalent to a lifetime of 15 hours to all species. All the rates and concentration are averaged for the daytime period between 10:00 and 15:00.

The modelled OH, HO_2 and RO_2 change when the model was unconstrained to HONO were shown in Fig. S7. After evaluation, in LAM and OCM sectors, concentration changes for OH were 46.9% and 43.2%, for HO_2 were 38.3% and 34.3%, for RO_2 were 43.7% and 39.0%, respectively. After evaluation, the $P(\text{Ox})$ was found to be 33% and 39% lower during the LAM and OCM periods, respectively. The nitric acid ($P(\text{HNO}_3)$) and sulfuric acid ($P(\text{H}_2\text{SO}_4)$) formation rates also increased simultaneously (~43% and ~48% for LAM and OCM sectors, respectively), while the nitric acid and sulfuric acid formation rates were 52% and 35% lower, respectively.

The sensitivity test identified the privileged role of the HONO-related mechanisms in the OH chemistry, which resulted in a correlation between the efficient radical recycling and secondary pollution.

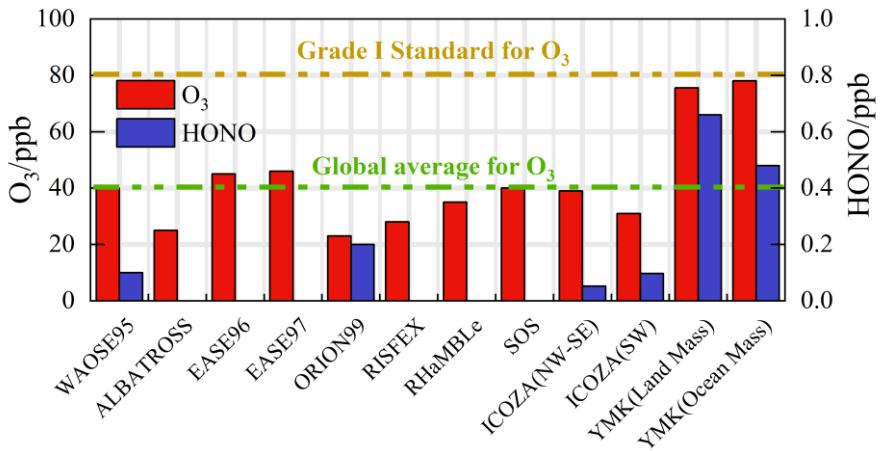
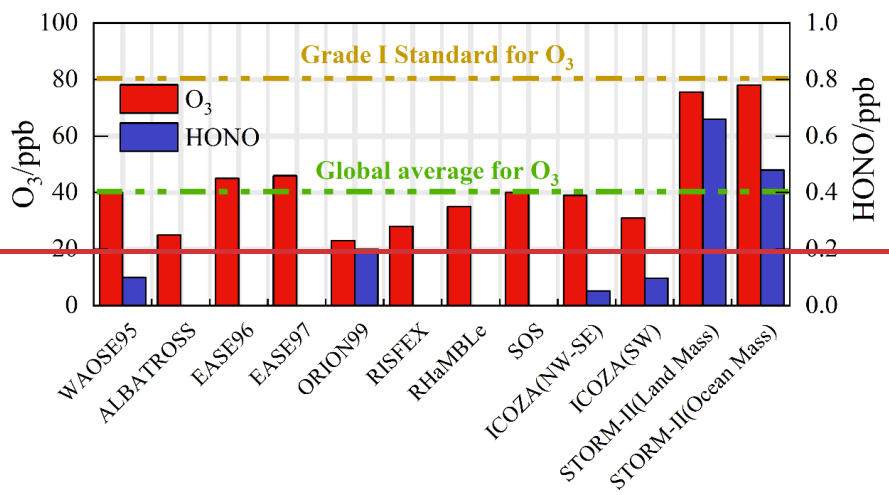


Fig. 149. Summary of both ozone and HONO concentrations in previous marine observations. The concentrations are averaged for the daytime period between 10:00 and 15:00.

A time-dependent box model was used to test the association between the HONO chemistry and the local ozone generation (Fig. 148(d)). In order to isolate the ~~the~~ O₃ photochemical production, the impacts of vertical entrainment and horizontal advection were in general ignored. On the basis of the base scenario run, constraints of the observed ozone and NO concentrations ~~was were~~ removed to predict ozone, ~~and the deposition process was equivalent to a lifetime of 15 hours to all species.~~ The observed and modelled O₃ concentrations in Fig. 148(d) are averaged for the daytime period between 10:00 and 15:00. The observed diurnal ozone concentrations were 75.7 ppb and 78.6 ppb during the LAM and OCM periods, respectively. The daytime ozone was well reproduced by the time-dependent box model, and the deviation of the simulation was less than 20% (Fig. 148(d)). After removing the HONO constraint, the simulated ozone concentrations were 38.2 and 26.3 ppb, i.e., 48% and 58% lower, during the LAM and OCM periods, respectively. Simulated O₃ decreased from ~75

856 ppb to a global background, and daytime HONO concentration were reduced to a low
857 level (~70 ppt)Both the HONO and ozone concentrations were reduced to a low level
858 (~70 ppt and ~35 ppb) and were close to several ocean observations (Fig. 11)
859 (Woodward-Massey et al., 2022b; Zhu et al., 2022; Xia et al., 2022). The elevated
860 daytime HONO had an additional effect on the oxidation in the background
861 atmosphere. For coastal cities, the particularity of the HONO chemistry in the MBL
862 tends to influence the ozone-sensitive system and eventually magnifies the ozone
863 background. Therefore, the promotion of oxidation by elevated precursor
864 concentrations is worth considering when formulating emission reduction policies. In
865 regions where HONO concentrations are elevated, the sources of HONO would need
866 to be identified to aid pollution mitigation policies.

867 5 Conclusions

868 Comprehensive observations of HOx radicals and other relevant species were
869 conducted in October 2019 at a coastal site in the Pearl River Delta (the YMK site,
870 22.55°N, 114.60°E). The overall air pollutants exhibited typical coastal features due to
871 the scarce anthropogenic emissions. The ~~average~~ daily maximum OH and HO₂
872 concentrations were $(4.7\text{--}9.5) \times 10^6 \text{ cm}^{-3}$ and $(4.2\text{--}8.1) \times 10^8 \text{ cm}^{-3}$, respectively. The
873 base RACM2-LIM1 model satisfactorily reproduced both the observed OH and HO₂
874 radical concentrations, but a slight overestimation of the OH radical occurred. The
875 daily maximum calculated total OH reactivity was 9.9 s^{-1} , and nearly 70% of the
876 reactivity was contributed by organic species.

877 In addition to anthropogenic and vegetation emissions, the synchronized air mass
878 transport from the northern cities and the South China Sea exerted a time-varying
879 influence on radical photochemistry and atmospheric oxidation. During the OCM
880 period, the observed OH and HO₂ radical concentrations could be reflected by the
881 base chemical mechanism, with daily average values of $4.5 \times 10^6 \text{ cm}^{-3}$ and 4.9×10^8
882 cm^{-3} , respectively. ~~The more active photochemical process during the LAM period~~
883 ~~promoted the underestimation of the radical concentrations. Unmeasured reactive~~

884 ~~species involved in oxidation propagation were responsible for elevated~~
885 ~~photochemistry.~~

886 In the episode that was dominated by ocean mass, the HO₂ + NO reaction
887 accounted for ~50% of the primary OH yield. A higher OH generation rate was
888 found(12.6 ppb/h) during the LAM period, and the secondary source accounted for 67%
889 of the total, which was similar to several observations in polluted plumes. Reactions
890 between RO_x and NO_x and self-combination were the main pathways of radical
891 termination (~70%), and the contribution of ~~peroxynitrateperoxynitrite~~ formation to
892 the L(RO_x) could not be ignored in the daytime.

893 Intensive photochemical reactions occur after the accumulation of precursors,
894 resulting in local net ozone production comparable to that in the surrounding suburban
895 environments. The daily average ozone production rates were 5.52 and 2.76 ppb/h in
896 the LAM and OCM periods, respectively. The rapid oxidation process was
897 accompanied by a higher diurnal HONO concentration (higher than 400 ppt). A non-
898 HONO-constrained sensitivity test was performed to quantify the HONO-induced
899 contribution to secondary pollution. After evaluation, the P(O_x) values were 33% and
900 39% lower during the LAM and OCM periods, respectively, ~~while the nitric acid and~~
901 ~~sulfuric acid formation rates were 52% and 35% lower, respectively. The nitric acid~~
902 ~~(P(HNO₃)) and sulfuric acid (P(H₂SO₄)) formation rates also increased~~
903 ~~simultaneously (~43% and ~48% for LAM and OCM sectors, respectively).~~
904 ~~Simulated O₃ decreased from ~75 ppb to a global background, and daytime HONO~~
905 ~~concentration were reduced to a low level (~70 ppt).The simulated daytime HONO~~
906 ~~and ozone concentrations were reduced to a low level (~70 ppt and ~35 ppb,~~
907 ~~respectively).~~ For coastal cities, the particularity of the HONO chemistry in the MBL
908 tends to influence the ozone-sensitive system and eventually magnifies the ozone
909 background. Therefore, the promotion of oxidation by elevated precursor
910 concentrations is worth considering when formulating emission reduction policies.

911 **Financial support**

912 This work was supported by the National Natural Science Foundation of China
913 (62275250, U19A2044, 61905003), the Natural Science Foundation of Anhui
914 Province (No. 2008085J20), the National Key R&D Program of China
915 (2022YFC3700301), and the Anhui Provincial Key R&D Program (2022107020022).

916 **Data availability**

917 The data used in this study are available from the corresponding author upon request
918 (rzhu@aiofm.ac.cn).

919 **Author contributions**

920 WQ Liu, PH Xie, RZ Hu contributed to the conception of this study. GX Zhang and
921 RZ Hu performed the data analyses and manuscript writing. All authors contributed to
922 measurements, discussed results, and commented on the paper.

923 **Competing interests**

924 The contact author has declared that none of the authors has any competing interests.

925

926

References

- 928 Bloss, W. J., Camredon, M., Lee, J. D., Heard, D. E., Plane, J. M. C., Saiz-Lopez, A., Bauguutte, S. J. B.,
929 Salmon, R. A., and Jones, A. E.: Coupling of HO_x, NO_x and halogen chemistry in the antarctic
930 boundary layer, *Atmos Chem Phys*, 10, 10187-10209, 10.5194/acp-10-10187-2010, 2010.
- 931 Brauers, T., Hausmann, M., Bister, A., Kraus, A., and Dorn, H.-P.: OH radicals in the boundary layer of
932 the Atlantic Ocean: 1. Measurements by long-path laser absorption spectroscopy, *Journal of*
933 *Geophysical Research*, 106, 7399, 10.1029/2000jd900679, 2001.
- 934 Carpenter, L. J., Fleming, Z. L., Read, K. A., Lee, J. D., Moller, S. J., Hopkins, J. R., Purvis, R. M.,
935 Lewis, A. C., Müller, K., Heinold, B., Herrmann, H., Fomba, K. W., van Pinxteren, D., Müller, C.,
936 Tegen, I., Wiedensohler, A., Müller, T., Niedermeier, N., Achterberg, E. P., Patey, M. D., Kozlova, E. A.,
937 Heimann, M., Heard, D. E., Plane, J. M. C., Mahajan, A., Oetjen, H., Ingham, T., Stone, D., Whalley, L.
938 K., Evans, M. J., Pilling, M. J., Leigh, R. J., Monks, P. S., Karunaharan, A., Vaughan, S., Arnold, S. R.,
939 Tschritter, J., Pöhler, D., Friß, U., Holla, R., Mendes, L. M., Lopez, H., Faria, B., Manning, A. J., and
940 Wallace, D. W. R.: Seasonal characteristics of tropical marine boundary layer air measured at the Cape
941 Verde Atmospheric Observatory, *J Atmos Chem*, 67, 87-140, 10.1007/s10874-011-9206-1, 2011.
- 942 Carslaw, N., Creasey, D. J., Heard, D. E., Lewis, A. C., McQuaid, J. B., Pilling, M. J., Monks, P. S.,
943 Bandy, B. J., and Penkett, S. A.: Modeling OH, HO₂, and RO₂radicals in the marine boundary layer: 1.
944 Model construction and comparison with field measurements, *Journal of Geophysical Research:*
945 *Atmospheres*, 104, 30241-30255, 10.1029/1999jd900783, 1999.
- 946 Chen, W., Guenther, A. B., Shao, M., Yuan, B., Jia, S., Mao, J., Yan, F., Krishnan, P., and Wang, X.:
947 Assessment of background ozone concentrations in China and implications for using region-specific
948 volatile organic compounds emission abatement to mitigate air pollution, *Environ Pollut*, 305, 119254,
949 10.1016/j.envpol.2022.119254, 2022.
- 950 Creasey, D. J., Heard, D. E., and Lee, J. D.: Eastern Atlantic Spring Experiment 1997 (EASE97) 1.
951 Measurements of OH and HO₂ concentrations at Mace Head, Ireland, *Journal of Geophysical Research:*
952 *Atmospheres*, 107, ACH 3-1-ACH 3-15, 10.1029/2001jd000892, 2002.
- 953 Crilley, L. R., Kramer, L. J., Pope, F. D., Reed, C., Lee, J. D., Carpenter, L. J., Hollis, L. D. J., Ball, S.
954 M., and Bloss, W. J.: Is the ocean surface a source of nitrous acid (HONO) in the marine boundary
955 layer?, *Atmos Chem Phys*, 21, 18213-18225, 10.5194/acp-21-18213-2021, 2021.
- 956 Fuchs, H., Dorn, H. P., Bachner, M., Bohn, B., Brauers, T., Gomm, S., Hofzumahaus, A., Holland, F.,
957 Nehr, S., Rohrer, F., Tillmann, R., and Wahner, A.: Comparison of OH concentration measurements by
958 DOAS and LIF during SAPHIR chamber experiments at high OH reactivity and low NO concentration,
959 *Atmos Meas Tech*, 5, 1611-1626, 10.5194/amt-5-1611-2012, 2012.
- 960 Fuchs, H., Tan, Z., Lu, K., Bohn, B., Broch, S., Brown, S. S., Dong, H., Gomm, S., Haeseler, R., He, L.,
961 Hofzumahaus, A., Holland, F., Li, X., Liu, Y., Lu, S., Min, K.-E., Rohrer, F., Shao, M., Wang, B., Wang,
962 M., Wu, Y., Zeng, L., Zhang, Y., Wahner, A., and Zhang, Y.: OH reactivity at a rural site (Wangdu) in
963 the North China Plain: contributions from OH reactants and experimental OH budget, *Atmos Chem*
964 *Phys*, 17, 645-661, 10.5194/acp-17-645-2017, 2017.
- 965 Grenfell, J. L., Savage, N. H., Harrison, R. M., Penkett, S. A., Forberich, O., Comes, F. J., Clemitshaw,
966 K. C., Burgess, R. A., Cardenas, L. M., Davison, B., and McFadyen, G. G.: Tropospheric box-
967 modelling and analytical studies of the hydroxyl (OH) radical and related species: Comparison with
968 observations, *J Atmos Chem*, 33, 183-214, 10.1023/a:1006009901180, 1999.

969 Griffith, S. M., Hansen, R. F., Dusanter, S., Stevens, P. S., Alaghmand, M., Bertman, S. B., Carroll, M.
970 A., Erickson, M., Galloway, M., Grossberg, N., Hottle, J., Hou, J., Jobson, B. T., Kammrath, A.,
971 Keutsch, F. N., Lefer, B. L., Mielke, L. H., O'Brien, A., Shepson, P. B., Thurlow, M., Wallace, W.,
972 Zhang, N., and Zhou, X. L.: OH and HO₂ radical chemistry during PROPHET 2008 and CABINEX
973 2009-Part 1: Measurements and model comparison, *Atmos Chem Phys*, 13, 5403-5423, 10.5194/acp-
974 13-5403-2013, 2013.

975 Hofzumahaus, A., Rohrer, F., Lu, K., Bohn, B., Brauers, T., Chang, C.-C., Fuchs, H., Holland, F., Kita,
976 K., Kondo, Y., Li, X., Lou, S., Shao, M., Zeng, L., Wahner, A., and Zhang, Y.: Amplified Trace Gas
977 Removal in the Troposphere, *Science*, 324, 1702-1704, 10.1126/science.1164566, 2009.

978 Huang, R. J., Hoffmann, T., Ovadnevaite, J., Laaksonen, A., Kokkola, H., Xu, W., Xu, W., Ceburnis, D.,
979 Zhang, R., Seinfeld, J. H., and O'Dowd, C.: Heterogeneous iodine-organic chemistry fast-tracks marine
980 new particle formation, *Proc Natl Acad Sci U S A*, 119, e2201729119, 10.1073/pnas.2201729119, 2022.

981 Jiang, Y., Xue, L., Shen, H., Dong, C., Xiao, Z., and Wang, W.: Dominant Processes of HONO Derived
982 from Multiple Field Observations in Contrasting Environments, *Environmental Science & Technology*
983 *Letters*, 10.1021/acs.estlett.2c00004, 2022.

984 Kanaya, Y., Sadanaga, Y., Nakamura, K., and Akimoto, H.: Behavior of OH and HO₂ radicals during
985 the Observations at a Remote Island of Okinawa (ORION99) field campaign 1. Observation using a
986 laser-induced fluorescence instrument, *J Geophys Res-Atmos*, 106, 24197-24208,
987 10.1029/2000jd000178, 2001.

988 Kanaya, Y., Yokouchi, Y., Matsumoto, J., Nakamura, K., Kato, S., Tanimoto, H., Furutani, H., Toyota,
989 K., and Akimoto, H.: Implications of iodine chemistry for daytime HO₂ levels at Rishiri Island,
990 *Geophys Res Lett*, 29, 45-41-45-44, 10.1029/2001gl014061, 2002.

991 Liu, C., Liu, G., Casazza, M., Yan, N., Xu, L., Hao, Y., Franzese, P. P., and Yang, Z.: Current Status and
992 Potential Assessment of China's Ocean Carbon Sinks, *Environ Sci Technol*, 56, 6584-6595,
993 10.1021/acs.est.1c08106, 2022a.

994 Liu, P., Xue, C., Ye, C., Liu, C., Zhang, C., Wang, J., Zhang, Y., Liu, J., and Mu, Y.: The Lack of
995 HONO Measurement May Affect the Accurate Diagnosis of Ozone Production Sensitivity, *ACS*
996 *Environmental Au*, 10.1021/acsenvironau.2c00048, 2022b.

997 Liu, T., Hong, Y., Li, M., Xu, L., Chen, J., Bian, Y., Yang, C., Dan, Y., Zhang, Y., Xue, L., Zhao, M.,
998 Huang, Z., and Wang, H.: Atmospheric oxidation capacity and ozone pollution mechanism in a coastal
999 city of southeastern China: analysis of a typical photochemical episode by an observation-based model,
1000 *Atmos Chem Phys*, 22, 2173-2190, 10.5194/acp-22-2173-2022, 2022c.

1001 Lou, S., Holland, F., Rohrer, F., Lu, K., Bohn, B., Brauers, T., Chang, C. C., Fuchs, H., Haseler, R.,
1002 Kita, K., Kondo, Y., Li, X., Shao, M., Zeng, L., Wahner, A., Zhang, Y., Wang, W., and Hofzumahaus, A.:
1003 Atmospheric OH reactivities in the Pearl River Delta – China in summer 2006: measurement and
1004 model results, *Atmos Chem Phys*, 10, 11243–11260, 10.5194/acp-10-11243-2010, 2010.

1005 Lu, K. D., Guo, S., Tan, Z. F., Wang, H. C., Shang, D. J., Liu, Y. H., Li, X., Wu, Z. J., Hu, M., and
1006 Zhang, Y. H.: Exploring atmospheric free-radical chemistry in China: the self-cleansing capacity and
1007 the formation of secondary air pollution, *Natl. Sci. Rev.*, 6, 579-594, 10.1093/nsr/nwy073, 2019.

1008 Lu, K. D., Hofzumahaus, A., Holland, F., Bohn, B., Brauers, T., Fuchs, H., Hu, M., Haeseler, R., Kita,
1009 K., Kondo, Y., Li, X., Lou, S. R., Oebel, A., Shao, M., Zeng, L. M., Wahner, A., Zhu, T., Zhang, Y. H.,
1010 and Rohrer, F.: Missing OH source in a suburban environment near Beijing: observed and modelled
1011 OH and HO₂ concentrations in summer 2006, *Atmos Chem Phys*, 13, 1057-1080, 10.5194/acp-13-
1012 1057-2013, 2013.

1013 Lu, K. D., Rohrer, F., Holland, F., Fuchs, H., Bohn, B., Brauers, T., Chang, C. C., Haeseler, R., Hu, M.,
1014 Kita, K., Kondo, Y., Li, X., Lou, S. R., Nehr, S., Shao, M., Zeng, L. M., Wahner, A., Zhang, Y. H., and
1015 Hofzumahaus, A.: Observation and modelling of OH and HO₂ concentrations in the Pearl River Delta
1016 2006: a missing OH source in a VOC rich atmosphere, *Atmos Chem Phys*, 12, 1541-1569,
1017 10.5194/acp-12-1541-2012, 2012.

1018 Ma, X. F., Tan, Z. F., Lu, K. D., Yang, X. P., Liu, Y. H., Li, S. L., Li, X., Chen, S. Y., Novelli, A., Cho,
1019 C. M., Zeng, L. M., Wahner, A., and Zhang, Y. H.: Winter photochemistry in Beijing: Observation and
1020 model simulation of OH and HO₂ radicals at an urban site, *Sci Total Environ*, 685, 85-95,
1021 10.1016/j.scitotenv.2019.05.329, 2019.

1022 Mallik, C., Tomsche, L., Bourtsoukidis, E., Crowley, J. N., Derstroff, B., Fischer, H., Hafermann, S.,
1023 Hüser, I., Javed, U., Keßel, S., Lelieveld, J., Martinez, M., Meusel, H., Novelli, A., Phillips, G. J.,
1024 Pozzer, A., Reiffs, A., Sander, R., Taraborrelli, D., Sauvage, C., Schuladen, J., Su, H., Williams, J., and
1025 Harder, H.: Oxidation processes in the eastern Mediterranean atmosphere: evidence from the modelling
1026 of HO_x; measurements over Cyprus, *Atmos Chem Phys*, 18, 10825-10847, 10.5194/acp-18-10825-
1027 2018, 2018.

1028 Niu, Y. B., Zhu, B., He, L. Y., Wang, Z., Lin, X. Y., Tang, M. X., and Huang, X. F.: Fast Nocturnal
1029 Heterogeneous Chemistry in a Coastal Background Atmosphere and Its Implications for Daytime
1030 Photochemistry, *Journal of Geophysical Research: Atmospheres*, 127, 10.1029/2022jd036716, 2022.

1031 Peng, X., Wang, W. H., Xia, M., Chen, H., Ravishankara, A. R., Li, Q. Y., Saiz-Lopez, A., Liu, P. F.,
1032 Zhang, F., Zhang, C. L., Xue, L. K., Wang, X. F., George, C., Wang, J. H., Mu, Y. J., Chen, J. M., and
1033 Wang, T.: An unexpected large continental source of reactive bromine and chlorine with significant
1034 impact on wintertime air quality, *Natl. Sci. Rev.*, 8, 10.1093/nsr/nwaa304, 2021.

1035 Qi, B., Kanaya, Y., Takami, A., Hatakeyama, S., Kato, S., Sadanaga, Y., Tanimoto, H., and Kajii, Y.:
1036 Diurnal peroxy radical chemistry at a remote coastal site over the sea of Japan, *Journal of Geophysical
1037 Research*, 112, 10.1029/2006jd008236, 2007.

1038 Slater, E. J., Whalley, L. K., Woodward-Massey, R., Ye, C., Lee, J. D., Squires, F., Hopkins, J. R.,
1039 Dunmore, R. E., Shaw, M., Hamilton, J. F., Lewis, A. C., Crilley, L. R., Kramer, L., Bloss, W., Vu, T.,
1040 Sun, Y., Xu, W., Yue, S., Ren, L., Acton, W. J. F., Hewitt, C. N., Wang, X., Fu, P., and Heard, D. E.:
1041 Elevated levels of OH observed in haze events during wintertime in central Beijing, *Atmos Chem Phys*,
1042 20, 14847-14871, 10.5194/acp-20-14847-2020, 2020.

1043 Song, H., Lu, K., Dong, H., Tan, Z., Chen, S., Zeng, L., and Zhang, Y.: Reduced Aerosol Uptake of
1044 Hydroperoxyl Radical May Increase the Sensitivity of Ozone Production to Volatile Organic
1045 Compounds, *Environmental Science & Technology Letters*, 9, 22-29, 10.1021/acs.estlett.1c00893,
1046 2021.

1047 Stockwell, W. R., Kirchner, F., Kuhn, M., and Seefeld, S.: A new mechanism for regional atmospheric
1048 chemistry modeling, *J Geophys Res-Atmos*, 102, 25847-25879, 10.1029/97jd00849, 1997.

1049 Stone, D., Whalley, L. K., and Heard, D. E.: Tropospheric OH and HO₂ radicals: field measurements
1050 and model comparisons, *Chemical Society reviews*, 41, 6348-6404, 10.1039/c2cs35140d, 2012.

1051 Sun, L., Chen, T., Jiang, Y., Zhou, Y., Sheng, L., Lin, J., Li, J., Dong, C., Wang, C., Wang, X., Zhang,
1052 Q., Wang, W., and Xue, L.: Ship emission of nitrous acid (HONO) and its impacts on the marine
1053 atmospheric oxidation chemistry, *Sci Total Environ*, 735, 139355, 10.1016/j.scitotenv.2020.139355,
1054 2020.

1055 Tan, Z., Lu, K., Ma, X., Chen, S., He, L., Huang, X., Li, X., Lin, X., Tang, M., Yu, D., Wahner, A., and
1056 Zhang, Y.: Multiple Impacts of Aerosols on O(3) Production Are Largely Compensated: A Case Study

1057 Shenzhen, China, *Environ Sci Technol*, 10.1021/acs.est.2c06217, 2022.

1058 Tan, Z., Lu, K., Jiang, M., Su, R., Wang, H., Lou, S., Fu, Q., Zhai, C., Tan, Q., Yue, D., Chen, D., Wang,
1059 Z., Xie, S., Zeng, L., and Zhang, Y.: Daytime atmospheric oxidation capacity in four Chinese
1060 megacities during the photochemically polluted season: a case study based on box model simulation,
1061 *Atmos Chem Phys*, 19, 3493-3513, 10.5194/acp-19-3493-2019, 2019a.

1062 Tan, Z. F., Lu, K. D., Dong, H. B., Hu, M., Li, X., Liu, Y. H., Lu, S. H., Shao, M., Su, R., Wang, H. C.,
1063 Wu, Y. S., Wahner, A., and Zhang, Y. H.: Explicit diagnosis of the local ozone production rate and the
1064 ozone-NO_x-VOC sensitivities, *Sci. Bull.*, 63, 1067-1076, 10.1016/j.scib.2018.07.001, 2018.

1065 Tan, Z. F., Lu, K. D., Hofzumahaus, A., Fuchs, H., Bohn, B., Holland, F., Liu, Y. H., Rohrer, F., Shao,
1066 M., Sun, K., Wu, Y. S., Zeng, L. M., Zhang, Y. S., Zou, Q., Kiendler-Scharr, A., Wahner, A., and Zhang,
1067 Y. H.: Experimental budgets of OH, HO₂, and RO₂ radicals and implications for ozone formation in
1068 the Pearl River Delta in China 2014, *Atmos Chem Phys*, 19, 7129-7150, 10.5194/acp-19-7129-2019,
1069 2019b.

1070 Tan, Z. F., Fuchs, H., Lu, K. D., Hofzumahaus, A., Bohn, B., Broch, S., Dong, H. B., Gomm, S.,
1071 Haseler, R., He, L. Y., Holland, F., Li, X., Liu, Y., Lu, S. H., Rohrer, F., Shao, M., Wang, B. L., Wang,
1072 M., Wu, Y. S., Zeng, L. M., Zhang, Y. S., Wahner, A., and Zhang, Y. H.: Radical chemistry at a rural
1073 site (Wangdu) in the North China Plain: observation and model calculations of OH, HO₂ and RO₂
1074 radicals, *Atmos Chem Phys*, 17, 663-690, 10.5194/acp-17-663-2017, 2017.

1075 Vaughan, S., Ingham, T., K. Whalley, L., Stone, D., Evans, M. J., Read, K. A., Lee, J. D., Moller, S. J.,
1076 Carpenter, L. J., Lewis, A. C., Fleming, Z. L., and Heard, D. E.: Seasonal observations of OH and HO₂
1077 in the remote tropical marine boundary layer, *Atmos. Chem. Phys.*, 12, 2149–2172, 10.5194/acp-12-
1078 2149-2012, 2012.

1079 Wang, F., Hu, R., Xie, P., Wang, Y., Chen, H., Zhang, G., and Liu, W.: Calibration source for OH
1080 radical based on synchronous photolysis, *Acta Phys Sin-Ch Ed*, 69, 2020.

1081 Wang, F. Y., Hu, R. Z., Chen, H., Xie, P. H., Wang, Y. H., Li, Z. Y., Jin, H. W., Liu, J. G., and Liu, W. Q.:
1082 Development of a field system for measurement of tropospheric OH radical using laser-induced
1083 fluorescence technique, *Opt. Express*, 27, A419-A435, 10.1364/oe.27.00a419, 2019.

1084 Wang, J., Zhang, Y., Zhang, C., Wang, Y., Zhou, J., Whalley, L. K., Slater, E. J., Dyson, J. E., Xu, W.,
1085 Cheng, P., Han, B., Wang, L., Yu, X., Wang, Y., Woodward-Massey, R., Lin, W., Zhao, W., Zeng, L.,
1086 Ma, Z., Heard, D. E., and Ye, C.: Validating HONO as an Intermediate Tracer of the External Cycling
1087 of Reactive Nitrogen in the Background Atmosphere, *Environ Sci Technol*, 10.1021/acs.est.2c06731,
1088 2023.

1089 Wang, T., Wei, X. L., Ding, A. J., Poon, C. N., Lam, K. S., Li, Y. S., Chan, L. Y., and Anson, M.:
1090 Increasing surface ozone concentrations in the background atmosphere of Southern China, 1994-2007,
1091 *Atmos Chem Phys*, 9, 6217-6227, 10.5194/acp-9-6217-2009, 2009.

1092 Wang, Y., Hu, R., Xie, P., Chen, H., Wang, F., Liu, X., Liu, J., and Liu, W.: Measurement of
1093 tropospheric HO₂ radical using fluorescence assay by gas expansion with low interferences, *J Environ
1094 Sci (China)*, 99, 40-50, 10.1016/j.jes.2020.06.010, 2021.

1095 Whalley, L. K., Furneaux, K. L., Goddard, A., Lee, J. D., Mahajan, A., Oetjen, H., Read, K. A., Kaaden,
1096 N., Carpenter, L. J., Lewis, A. C., Plane, J. M. C., Saltzman, E. S., Wiedensohler, A., and Heard, D. E.:
1097 The chemistry of OH and HO₂ radicals in the boundary layer over the tropical Atlantic Ocean, *Atmos
1098 Chem Phys*, 10, 1555-1576, 2010.

1099 Woodward-Massey, R., Sommariva, R., Whalley, L. K., Cryer, D. R., Ingham, T., Bloss, W. J., Ball, S.
1100 M., Lee, J. D., Reed, C. P., Crilley, L. R., Kramer, L. J., Bandy, B. J., Forster, G. L., Reeves, C. E.,

1101 Monks, P. S., and Heard, D. E.: Radical chemistry at a UK coastal receptor site – Part 2: experimental
1102 radical budgets and ozone production, *Atmos. Chem. Phys.*, 10.5194/acp-2022-213, 2022a.

1103 Woodward-Massey, R., Sommariva, R., Whalley, L. K., Cryer, D. R., Ingham, T., Bloss, W. J., Ball, S.
1104 M., Lee, J. D., Reed, C. P., Crilley, L. R., Kramer, L. J., Bandy, B. J., Forster, G. L., Reeves, C. E.,
1105 Monks, P. S., and Heard, D. E.: Radical chemistry at a UK coastal receptor site – Part 1: observations
1106 of OH, HO₂, RO₂, and OH reactivity and comparison to MCM model predictions, *Atmos. Chem. Phys.*,
1107 10.5194/acp-2022-207, 2022b.

1108 Xia, M., Wang, T., Wang, Z., Chen, Y., Peng, X., Huo, Y., Wang, W., Yuan, Q., Jiang, Y., Guo, H., Lau,
1109 C., Leung, K., Yu, A., and Lee, S.: Pollution-Derived Br₂ Boosts Oxidation Power of the Coastal
1110 Atmosphere, *Environ Sci Technol*, 10.1021/acs.est.2c02434, 2022.

1111 Xia, S.-Y., Zhu, B., Wang, S.-X., Huang, X.-F., and He, L.-Y.: Spatial distribution and source
1112 apportionment of peroxyacetyl nitrate (PAN) in a coastal region in southern China, *Atmos Environ*, 260,
1113 10.1016/j.atmosenv.2021.118553, 2021.

1114 Xu, W., Ovadnevaite, J., Fossum, K. N., Lin, C., Huang, R.-J., Ceburnis, D., and O’Dowd, C.: Sea
1115 spray as an obscured source for marine cloud nuclei, *Nature Geoscience*, 15, 282-286, 10.1038/s41561-
1116 022-00917-2, 2022.

1117 Yang, X., Lu, K., Ma, X., Gao, Y., Tan, Z., Wang, H., Chen, X., Li, X., Huang, X., He, L., Tang, M.,
1118 Zhu, B., Chen, S., Dong, H., Zeng, L., and Zhang, Y.: Radical chemistry in the Pearl River Delta:
1119 observations and 2 modeling of OH and HO₂ radicals in Shenzhen 2018, 10.5194/acp-2022-113, 2022a.

1120 Yang, X., Lu, K., Ma, X., Gao, Y., Tan, Z., Wang, H., Chen, X., Li, X., Huang, X., He, L., Tang, M.,
1121 Zhu, B., Chen, S., Dong, H., Zeng, L., and Zhang, Y.: Radical chemistry in the Pearl River Delta:
1122 observations and modeling of OH and HO₂ radicals in Shenzhen in 2018, *Atmos Chem Phys*, 22,
1123 12525-12542, 10.5194/acp-22-12525-2022, 2022b.

1124 Yang, X., Lu, K., Ma, X., Liu, Y., Wang, H., Hu, R., Li, X., Lou, S., Chen, S., Dong, H., Wang, F.,
1125 Wang, Y., Zhang, G., Li, S., Yang, S., Yang, Y., Kuang, C., Tan, Z., Chen, X., Qiu, P., Zeng, L., Xie, P.,
1126 and Zhang, Y.: Observations and modeling of OH and HO₂ radicals in Chengdu, China in summer
1127 2019, *The Science of the total environment*, 772, 144829-144829, 10.1016/j.scitotenv.2020.144829,
1128 2021a.

1129 Yang, Y., Li, X., Zu, K., Lian, C., Chen, S., Dong, H., Feng, M., Liu, H., Liu, J., Lu, K., Lu, S., Ma, X.,
1130 Song, D., Wang, W., Yang, S., Yang, X., Yu, X., Zhu, Y., Zeng, L., Tan, Q., and Zhang, Y.: Elucidating
1131 the effect of HONO on O₃ pollution by a case study in southwest China, *Sci Total Environ*, 756,
1132 144127, 10.1016/j.scitotenv.2020.144127, 2021b.

1133 Zeren, Y., Zhou, B., Zheng, Y., Jiang, F., Lyu, X., Xue, L., Wang, H., Liu, X., and Guo, H.: Does Ozone
1134 Pollution Share the Same Formation Mechanisms in the Bay Areas of China?, *Environ Sci Technol*,
1135 10.1021/acs.est.2c05126, 2022.

1136 Zhang, G., Hu, R., Xie, P., Lou, S., Wang, F., Wang, Y., Qin, M., Li, X., Liu, X., Wang, Y., and Liu, W.:
1137 Observation and simulation of HO_x radicals in an urban area in Shanghai, China, *Sci Total Environ*,
1138 810, 152275, 10.1016/j.scitotenv.2021.152275, 2022a.

1139 Zhang, G., Hu, R., Xie, P., Lu, K., Lou, S., Liu, X., Li, X., Wang, F., Wang, Y., Yang, X., Cai, H., Wang,
1140 Y., and Liu, W.: Intercomparison of OH radical measurement in a complex atmosphere in Chengdu,
1141 China, *Sci Total Environ*, 155924, 10.1016/j.scitotenv.2022.155924, 2022b.

1142 Zhu, B., Huang, X.-F., Xia, S.-Y., Lin, L.-L., Cheng, Y., and He, L.-Y.: Biomass-burning emissions
1143 could significantly enhance the atmospheric oxidizing capacity in continental air pollution, *Environ.*
1144 *Pollut.*, 285, 10.1016/j.envpol.2021.117523, 2021.

1145 Zhu, J., Wang, S., Wang, H., Jing, S., Lou, S., Saiz-Lopez, A., and Zhou, B.: Observationally
1146 constrained modeling of atmospheric oxidation capacity and photochemical reactivity in Shanghai,
1147 China, *Atmos Chem Phys*, 20, 1217-1232, 10.5194/acp-20-1217-2020, 2020.
1148 Zhu, Y., Wang, Y., Zhou, X., Elshorbany, Y. F., Ye, C., Hayden, M., and Peters, A. J.: An investigation
1149 into the chemistry of HONO in the marine boundary layer at Tudor Hill Marine Atmospheric
1150 Observatory in Bermuda, *Atmos Chem Phys*, 22, 6327-6346, 10.5194/acp-22-6327-2022, 2022.
1151 Zou, Z., Chen, Q., Xia, M., Yuan, Q., Chen, Y., Wang, Y., Xiong, E., Wang, Z., and Wang, T.: OH
1152 measurements in the coastal atmosphere of South China: missing OH sinks in aged air masses,
1153 *EGUsphere*, 2022, 1-47, 10.5194/egusphere-2022-854, 2022.
1154